EUROPEAN ORGANISATION FOR NUCLEAR RESEARCH (CERN)

Submitted to: Phys. Rev. D

CERN-EP-2022-044
January 27, 2023

Search for flavor-changing neutral-current couplings between the top quark and the Z boson with LHC Run 2 proton–proton collisions at $\sqrt{s} = 13$ TeV with the ATLAS detector

The ATLAS Collaboration

A search for flavor-changing neutral-current couplings between a top quark, an up or charm quark and a Z boson is presented, using proton–proton collision data at $\sqrt{s} = 13$ TeV collected by the ATLAS detector at the Large Hadron Collider. The analyzed dataset corresponds to an integrated luminosity of 139 fb^{-1}. The search targets both single-top-quark events produced as $gq \to tZ$ (with $q = u, c$) and top-quark-pair events, with one top quark decaying through the $t \to Zq$ channel. The analysis considers events with three leptons (electrons or muons), a b-tagged jet, possible additional jets, and missing transverse momentum. The data are found to be consistent with the background-only hypothesis and 95% confidence-level limits on the $t \to Zq$ branching ratios are set, assuming only tensor operators of the Standard Model effective field theory framework contribute to the tZq vertices. These are 6.2×10^{-5} (13×10^{-5}) for $t \to Zu$ ($t \to Zc$) for a left-handed tZq coupling, and 6.6×10^{-5} (12×10^{-5}) in the case of a right-handed coupling. These results are interpreted as 95% CL upper limits on the strength of corresponding couplings, yielding limits for $|C_{uW}^{(13)*}|$ and $|C_{uB}^{(13)*}|$ ($|C_{uW}^{(31)}|$ and $|C_{uB}^{(31)}|$) of 0.15 (0.16), and limits for $|C_{uW}^{(23)*}|$ and $|C_{uB}^{(23)*}|$ ($|C_{uW}^{(32)}|$ and $|C_{uB}^{(32)}|$) of 0.22 (0.21), assuming a new-physics energy scale Λ_{NP} of 1 TeV.

Contents

1 Introduction

The top quark is the heaviest elementary particle known and it decays almost exclusively into Wb [1]. In the Standard Model of particle physics (SM), flavor-changing neutral-current (FCNC) processes involving a top quark, an up-type quark and a Z boson are forbidden at tree level and are strongly suppressed by the GIM mechanism [2] at higher orders, leading to branching ratios for top-quark decays via FCNC processes of the order of 10^{-14} [3]. However, several SM extensions predict such branching ratios to be between 10^{-4} and 10^{-7}. Examples of SM extensions are the quark-singlet model [4], the two-Higgs-doublet model [5], the Minimal Supersymmetric Standard Model (MSSM) [6], the MSSM with R-parity violation [7], models with warped extra dimensions [8], and extended mirror fermion models [9].

FCNC couplings can be described by an effective field theory (EFT) [10, 11] that extends the SM Lagrangian $\mathcal{L}_{\text{SM}}$ with higher-dimensional operators suppressed by the scale of new physics, Λ_{NP}, as shown in Eq. (1). At order Λ_{NP}^{-2} the strength of the anomalous couplings is given by the Wilson coefficients C_k that multiply dimension-six operators O_k,

$$\mathcal{L}_{\text{eff}} = \mathcal{L}_{\text{SM}} + \frac{1}{\Lambda_{\text{NP}}^2} \sum_k C_k O_k . \tag{1}$$

The relevant operators for an FCNC process with a top quark and a Z boson, following the notation in Ref. [12], are the operators $O_{uB}^{(ij)}$ and $O_{uW}^{(ij)}$ with $i \neq j$. The indices i and j of the operators refer to the flavor indices of the quark generations. One index is always equal to 3 as a top quark must be involved, while the other one is either 1 or 2, corresponding to an up or charm quark. The FCNC tZq interactions can be introduced by vector and tensor couplings, but only the latter are considered in this analysis because they would produce most of the "FCNC-in-single-top-production" signal [11]. The FCNC operators can be left-handed (LH) or right-handed (RH). The order of the indices i and j in Eq. (1) defines the chirality

of the FCNC operators. A linear combination of the $C_{uB}^{(13)}$ and $C_{uW}^{(13)}$ coefficients corresponds to the tZu LH coupling while a linear combination of the $C_{uB}^{(31)}$ and $C_{uW}^{(31)}$ coefficients defines the tZu RH coupling. Similarly, the tZc couplings are defined by the $C_{uB}^{(23)}$ and $C_{uW}^{(23)}$ coefficients for the LH case, while the $C_{uB}^{(32)}$ and $C_{uW}^{(32)}$ coefficients describe the RH case. For each linear combination, the two coefficients assume the same value with an opposite sign [11].

Experimental limits on the branching ratio of FCNC $t \to Zq$ decays were previously established by experiments at the Large Electron–Positron Collider (LEP) [13–16], the Hadron–Electron Ring Accelerator (HERA) [17], the Tevatron [18, 19] and the Large Hadron Collider (LHC) [20–23]. The most stringent observed limits, $\mathcal{B}(t \to Zu) < 17 \times 10^{-5}$ and $\mathcal{B}(t \to Zc) < 24 \times 10^{-5}$ [21], were set by ATLAS in a search for FCNC processes in $t\bar{t}$ decays only, using 36.1 fb^{-1} of pp collision data at $\sqrt{s} = 13$ TeV. The quoted limits apply to both the left- and right-handed couplings, as the analysis is not sensitive to the chirality.

This paper presents a search for FCNC tZq couplings, using pp collision data at $\sqrt{s} = 13$ TeV collected by the ATLAS experiment at the LHC and corresponding to an integrated luminosity of 139 fb^{-1}. The search is performed by analyzing the top-quark decays in $t\bar{t}$ events as well as the production of single top quarks, as illustrated in Figure 1. In the former channel, one of the top quarks decays through an FCNC process ($t \to Zq$) and the other through the dominant mode ($t \to Wb$). In contrast, in the latter channel the production of a single top quark proceeds through an FCNC process ($gq \to tZ$). Single top production with FCNC decay contributes negligibly and is not considered in this analysis. While single top-quark production gives the analysis more sensitivity to the FCNC tZu coupling, the $t\bar{t}$ decay mode provides almost equal sensitivity to the FCNC tZu and tZc couplings. Since the FCNC production and decay processes are induced by the same couplings, the production cross-section and decay branching ratio are connected. Therefore, the FCNC single-top production cross-section can be interpreted as the branching ratio of the corresponding FCNC decay. Thus, the analysis results for the numbers of production and decay signal events are translated into branching ratios for $t \to Zq$. For both of the considered channels, only the trileptonic final state is selected, in which the Z boson decays into charged leptons and the W boson from the top quark decays leptonically. The final states where either the Z boson or the W boson decays hadronically are not considered because of the larger backgrounds. Therefore, the analysis selects events with three leptons (electrons or muons), a b-tagged jet, possible additional jets, and missing transverse momentum. After the selection, the main background sources are diboson, $t\bar{t}Z$ and tZ production. To improve the separation of signal from background events, a multivariate technique is used, which was not employed in the previous analysis. The statistical analysis uses a binned profile likelihood fit to the data.

2 ATLAS detector

The ATLAS experiment [24] at the LHC is a multipurpose particle detector with a forward–backward symmetric cylindrical geometry and a near 4π coverage in solid angle.[1] It consists of an inner tracking detector surrounded by a thin superconducting solenoid providing a 2 T axial magnetic field, electromagnetic and

[1] ATLAS uses a right-handed coordinate system with its origin at the nominal interaction point (IP) in the center of the detector and the z-axis along the beam pipe. The x-axis points from the IP to the center of the LHC ring, and the y-axis points upwards. Cylindrical coordinates (r, ϕ) are used in the transverse plane, ϕ being the azimuthal angle around the z-axis. The pseudorapidity is defined in terms of the polar angle θ as $\eta = -\ln\tan(\theta/2)$. Distances in the η–ϕ plane are measured in units of $\Delta R \equiv \sqrt{(\Delta\eta)^2 + (\Delta\phi)^2}$.

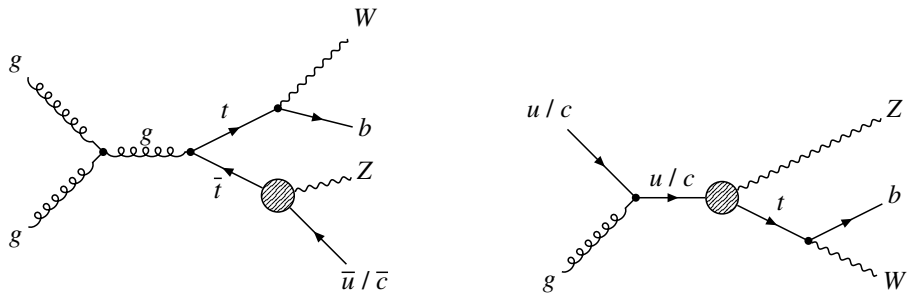

(a) (b)

Figure 1: Examples of the lowest-order Feynman diagrams for (a) $t\bar{t}$ production, with one top quark decaying through the dominant mode in the SM and the other via an FCNC process and for (b) single top-quark production via an FCNC process in the s-channel.

hadron calorimeters, and a muon spectrometer. The inner tracking detector (ID) covers the pseudorapidity range $|\eta| < 2.5$. It consists of silicon pixel, silicon microstrip, and transition radiation tracking detectors. Lead/liquid-argon (LAr) sampling calorimeters provide electromagnetic (EM) energy measurements with high granularity. A steel/scintillator-tile hadron calorimeter covers the central pseudorapidity range ($|\eta| < 1.7$). The endcap and forward regions are instrumented with LAr calorimeters for both the EM and hadronic energy measurements up to $|\eta| = 4.9$. The muon spectrometer surrounds the calorimeters and is based on three large superconducting air-core toroidal magnets with eight coils each. The field integral of the toroids ranges between 2.0 and 6.0 T m across most of the detector. The muon spectrometer includes a system of precision tracking chambers and fast detectors for triggering. A two-level trigger system [25] is used to select events. The first-level trigger is implemented in hardware and uses a subset of the detector information to accept events at a rate below 100 kHz. This is followed by a software-based trigger that reduces the accepted event rate to 1 kHz on average depending on the data-taking conditions. An extensive software suite [26] is used in data simulation, in the reconstruction and analysis of real and simulated data, in detector operations, and in the trigger and data acquisition systems of the experiment.

3 Data and samples of simulated events

The data sample used in this analysis corresponds to 139 fb^{-1} of pp collisions at $\sqrt{s} = 13$ TeV collected by the ATLAS detector during 2015–2018, after requiring stable LHC beams and that all detector subsystems were operational [27].

Candidate events were required to satisfy one of the single-electron triggers or one of the single-muon triggers [25, 28, 29]. Single-lepton triggers with low transverse momentum (p_{T}) thresholds and isolation requirements were combined in a logical OR with higher-threshold triggers that had a looser identification criterion and did not have any isolation requirement. The lowest p_{T} threshold used for electrons was 24 GeV (26 GeV) in 2015 (2016–2018), while for muons the corresponding threshold was 20 GeV (26 GeV).

To evaluate the effects of the detector resolution and acceptance on the signal and background, and to estimate the SM backgrounds, simulated event samples were produced using a GEANT4-based Monte Carlo (MC) detector simulation [30, 31]. Some of the samples used for evaluating systematic uncertainties did not use the full GEANT4 simulation but instead relied on parameterized showers in the calorimeter [31].

The top-quark mass in the event generators described below was set to $m_t = 172.5$ GeV. In all samples, the decays of bottom and charm hadrons were performed by EvtGen 1.2.0 [32], unless stated otherwise.

The simulated data must account for the fact that significantly more than one inelastic pp collision occurs per bunch crossing. The average number of collisions per bunch crossing ranged from 13 to 38 for the 2015–2018 data-taking periods. Inelastic collisions were simulated using Pythia 8.186 [33] with the A3 set of tuned parameters [34] and the NNPDF2.3lo [35] set of parton distribution functions (PDFs), and overlaid on the signal and background MC samples. These simulated events were reweighted to match the conditions of the collision data, specifically the number of additional pp interactions in the same and neighboring bunch crossings (pileup).

Several MC signal event samples were generated at next-to-leading order (NLO) in QCD with MadGraph5_aMC@NLO 2.7.2 [36], using the NNPDF3.0nlo [37] PDF set. Parton showering and hadronization were modeled with Pythia 8.302 with the NNPDF2.3lo PDF set and the A14 set of tuned parameters [38]. Only events with leptonic decays (including τ-leptons) of the W and Z bosons were generated. The TopFCNC Universal FeynRules Output (UFO) model [11, 39, 40] was used for the computation of top-quark FCNC production and decay processes at NLO in QCD. Since FCNC processes in both production and decay are considered in this analysis, separate samples for each mode and for tZu and tZc couplings were generated. In order to study the chirality of these couplings, separate samples with LH and RH couplings were produced.

Additional signal samples generated with the same version of MadGraph5_aMC@NLO were interfaced to Herwig 7.1.6 [41, 42] instead of Pythia 8.302 to assess the uncertainty related to the choice of parton-shower model. The Herwig 7.1 default set of tuned parameters [42, 43] was used together with the MMHT2014lo PDF set [44]. The decays of bottom and charm hadrons were performed by EvtGen 1.7.0.

For the normalization, the branching ratios are set to the best observed limits reported in Section 1, constraining $\mathcal{B}(t \to q'W) = 1 - \mathcal{B}(t \to uZ/cZ)$, with $q' = d, s, b$. The FCNC $t\bar{t}$ decay signal is normalized using the $t\bar{t}$ cross-section prediction at next-to-next-to-leading order (NNLO) in QCD including the resummation of next-to-next-to-leading logarithmic (NNLL) soft-gluon terms calculated using Top++ 2.0 [45–51]. The FCNC single top-quark production signal normalization cross-section is calculated at NLO using the TopFCNC model as implemented in MadGraph5_aMC@NLO.

The background is estimated using simulated samples that contain at least two leptons and at least two jets. These samples include the production of $t\bar{t}$, $t\bar{t}H$, $t\bar{t}Z$, $t\bar{t}W$, tZ, tW, tWZ, Z + jets, diboson, triboson, $t\bar{t}t$, $t\bar{t}t\bar{t}$, $t\bar{t}WW$, ZH and WH events.

The production of $t\bar{t}$ and $t\bar{t}H$ events was modeled using the Powheg Box v2 [52–56] generator at NLO with the NNPDF3.0nlo PDF set and the h_{damp} parameter[2] set to $1.5\, m_t$ for $t\bar{t}$ [57] and to $0.75 \times (2\, m_t + m_H)$ for $t\bar{t}H$, with $m_H = 125$ GeV. The events were interfaced to Pythia 8.230 [58] to model the parton shower, hadronization, and underlying event, with parameters set according to the A14 tune and using the NNPDF2.3lo set of PDFs. The decays of bottom and charm hadrons were performed by EvtGen 1.6.0.

Additional $t\bar{t}$ simulated samples are used to assess modeling uncertainties [59]. The impact of using a different parton shower and hadronization model is evaluated by comparing the nominal "Powheg+Pythia" $t\bar{t}$ sample with another event sample produced with the Powheg Box v2 generator, but interfaced with Herwig 7.1.3, which used the Herwig 7.1 default set of tuned parameters and the MMHT2014lo PDF set.

[2] The h_{damp} parameter is a resummation damping factor and one of the parameters that controls the matching of Powheg matrix elements to the parton shower and thus effectively regulates the high-p_{T} radiation against which the $t\bar{t}$ system recoils.

To estimate the systematic uncertainty in the choice of the h_{damp} parameter, a sample generated in the same way as the nominal one but with the h_{damp} parameter set to $3.0\,m_t$ was produced.

The production of $t\bar{t}Z$ and $t\bar{t}W$ events was modeled using the MadGraph5_aMC@NLO 2.3.3 generator at NLO with the NNPDF3.0nlo PDF set. The events were interfaced to Pythia 8.210, which used the A14 tune and the NNPDF2.3lo PDF set.

Additional $t\bar{t}Z$ simulated samples are used to assess modeling uncertainties. The impact of using a different parton shower and hadronization model is evaluated by comparing the nominal $t\bar{t}Z$ sample with an event sample produced with the MadGraph5_aMC@NLO 2.6.2 generator interfaced with Herwig 7.0.4, which used the Herwig 7.0 default set of tuned parameters and the MMHT2014lo PDF set. The decays of bottom and charm hadrons were performed by EvtGen 1.6.0. The uncertainty due to initial-state radiation (ISR) is estimated by comparing the nominal event sample with two samples where the Var3c [38] up and down variations of the A14 tune were employed.

The SM production of a single top quark in association with a Z boson (tZ) was modeled using the MadGraph5_aMC@NLO 2.3.3 generator at NLO with the NNPDF3.0nlo PDF set. The events were interfaced with Pythia 8.230, which used the A14 tune and the NNPDF2.3lo PDF set.

Similarly to $t\bar{t}Z$, additional tZ simulated samples are used to assess modeling uncertainties. The impact of using a different parton shower and hadronization model is evaluated by comparing the nominal tZ sample with an event sample produced with the MadGraph5_aMC@NLO 2.8.1 generator interfaced with Herwig 7.2.1, which used the Herwig 7.1 default set of tuned parameters and the MMHT2014lo PDF set. The decays of bottom and charm hadrons were performed by EvtGen 1.7.0. The uncertainty due to ISR is estimated by comparing the nominal tZ sample with two additional samples, which had the same settings as the nominal one, but employed the Var3c up and down variations of the A14 tune.

The associated production of a single top quark with a W boson (tW) was modeled by the Powheg Box v2 [60] generator at NLO in QCD using the five-flavor scheme and the NNPDF3.0nlo set of PDFs. The diagram removal (DR) scheme [61] was used to remove interference and overlap with $t\bar{t}$ production. The events were interfaced to Pythia 8.230, which used the A14 tune and the NNPDF2.3lo set of PDFs.

The production of tWZ events was modeled using the MadGraph5_aMC@NLO 2.3.3 generator at NLO with the NNPDF3.0nlo PDF set. The events were interfaced with Pythia 8.212, which used the A14 tune and the NNPDF2.3lo PDF set. The DR scheme was employed to handle the interference between the tWZ and $t\bar{t}Z$ processes. A sample with an alternative scheme described in Ref. [62] was produced to assess the associated systematic uncertainty.

The Powheg Box v1 MC generator [63] was used to simulate at NLO accuracy the hard-scattering processes of Z boson production and decay in the electron, muon, and τ-lepton channels. It was interfaced to Pythia 8.186 for the modeling of the parton shower, hadronization, and underlying event, with parameters set according to the AZNLO tune [64]. The CT10nlo [65] PDF set was used for the hard-scattering processes, whereas the CTEQ6L1 [66] PDF set was used for the parton shower. The effect of QED final-state radiation was simulated with Photos++ 3.52 [67, 68].

Samples of diboson final states (VV, with $V = W, Z$) were simulated with the Sherpa 2.2.1 or 2.2.2 [69] generator depending on the process, including off-shell effects and Higgs boson contributions where appropriate. Fully leptonic final states and semileptonic final states, where one boson decays leptonically and the other hadronically, were generated using matrix elements at NLO accuracy in QCD for up to one additional parton and at LO accuracy for up to three additional parton emissions. Samples for the loop-induced processes $gg \to VV$ were generated using LO-accurate matrix elements for up to one

additional parton emission for both the cases of fully leptonic and semileptonic final states. The matrix element calculations were matched and merged with the SHERPA parton shower based on Catani–Seymour dipole factorization [70, 71] using the MEPS@NLO prescription [72–75]. The virtual QCD corrections were provided by the OPENLOOPS library [76–78]. The NNPDF3.0NNLO set of PDFs was used, along with the dedicated set of tuned parton-shower parameters developed by the SHERPA authors. Electroweak production of a diboson in association with two jets ($VVjj$) was simulated with the SHERPA 2.2.2 generator. The LO-accurate matrix elements were matched to a parton shower based on Catani–Seymour dipole factorization using the MEPS@LO prescription. Samples were generated using the NNPDF3.0NNLO PDF set, along with the dedicated set of tuned parton-shower parameters developed by the SHERPA authors. The decays of bottom and charm hadrons are performed with built-in SHERPA features. An invariant mass of $m_{\ell\ell} > 4\,\text{GeV}$ was required at matrix-element level for any pair of same-flavor charged leptons.

To assess the uncertainty that the generator contributes to the simulation of diboson final states, alternative samples are employed. For these, the POWHEG BOX v2 [79] generator was used instead of SHERPA. The effect of singly resonant amplitudes and interference effects due to Z/γ^* and same-flavor lepton combinations in the final state were included where appropriate. Interference effects between WW and ZZ for same-flavor charged leptons and neutrinos were ignored. Events were interfaced to PYTHIA 8.186 for the modeling of the parton shower, hadronization, and underlying event, with parameters set according to the AZNLO tune. The CT10 PDF set was used for the hard-scattering processes, whereas the CTEQ6L1 PDF set was used for the parton shower. The factorization and renormalization scales were set to the invariant mass of the boson pair. The same invariant mass selection as for the SHERPA samples was applied.

The production of triboson (VVV, with $V = W, Z$) events was simulated with the SHERPA 2.2.2 generator. Matrix elements, accurate to NLO for the inclusive process and to LO for up to two additional parton emissions, were matched and merged with the SHERPA parton shower based on Catani–Seymour dipole factorization using the MEPS@NLO prescription. The virtual QCD corrections for matrix elements at NLO accuracy were provided by the OPENLOOPS library. Samples were generated using the NNPDF3.0NNLO PDF set, along with the dedicated set of tuned parton-shower parameters developed by the SHERPA authors. The decays of bottom and charm hadrons are performed with built-in SHERPA features.

The production of $t\bar{t}t\bar{t}$ events was modeled using the MADGRAPH5_AMC@NLO 2.6.2 generator at NLO with the NNPDF3.1NLO [37] PDF set. The events were interfaced with PYTHIA 8.230, which used the A14 tune and the NNPDF2.3LO PDF set. The decays of bottom and charm hadrons were simulated using the EVTGEN 1.6.0 program.

Other rare top-quark processes, namely the production of $t\bar{t}WW$ and $t\bar{t}t$ events, were modeled using the MADGRAPH5_AMC@NLO generator at LO interfaced with PYTHIA 8, which used the A14 tune. The associated production of a Higgs boson with a W or Z boson, VH, was modeled using PYTHIA 8.186 with the A14 tune and the NNPDF2.3LO PDF set.

Throughout the paper the various MC samples are merged or split as follows. The $t\bar{t}Z$ and tWZ backgrounds are combined. The diboson contribution is split according to the origin of the associated jets using generator-level information. Their origin is determined by matching, within a cone of size $\Delta R = 0.3$, jets to hadrons with $p_{\text{T}} > 5\,\text{GeV}$. If one of the jets contains a b- or c-hadron, then it is classified as diboson + heavy flavor (VV + HF), otherwise the event is classified as diboson + light flavor (VV + LF). The $t\bar{t}$, tW, Z + jets, VV and $t\bar{t}V$ processes with two prompt[3] leptons and one nonprompt or fake lepton (a jet

[3] Prompt leptons are leptons from the decay of W or Z bosons, either directly or through an intermediate $\tau \to \ell\nu\nu$ decay, or from the semileptonic decay of top quarks.

misidentified as a lepton) are shown together and called "Fakes". The other minor backgrounds, namely $t\bar{t}W$, $t\bar{t}H$, VH, $t\bar{t}WW$, triboson, $t\bar{t}t$ and $t\bar{t}t\bar{t}$, are merged and called "Other bkg.".

4 Object reconstruction

The reconstruction of the basic objects used in the analysis is described in the following. The primary vertex [80] is selected as the pp vertex candidate with the highest sum of the squared transverse momenta of all associated tracks with $p_{\mathrm{T}} > 500\,\mathrm{MeV}$.

Electron candidates are reconstructed from energy clusters in the EM calorimeter that match a reconstructed track [81]. The clusters are required to be within the range $|\eta| < 2.47$, excluding the transition region between the barrel and endcap calorimeters at $1.37 < |\eta| < 1.52$. Each electron candidate's transverse impact parameter relative to the beam axis, d_0, divided by its estimated uncertainty must satisfy $|d_0|/\sigma(d_0) < 5$, while the longitudinal distance z_0 from the reconstructed primary vertex to the point where d_0 is measured must satisfy $|z_0 \sin(\theta)| < 0.5\,\mathrm{mm}$. Electron candidates must also satisfy a transverse momentum requirement of $p_{\mathrm{T}} > 15\,\mathrm{GeV}$. A likelihood-based discriminant is constructed from a set of variables that enhance the electron selection, while rejecting photon conversions and hadrons misidentified as electrons. An η- and p_{T}-dependent selection on the likelihood discriminant is applied, and the "Medium" identification [81] is used. Electrons are also required to be isolated using criteria based on ID tracks. Nonprompt leptons are rejected using a boosted decision tree (BDT) discriminant based on isolation and b-tagging variables, referred to as the nonprompt-lepton BDT [82]. The efficiency at the chosen working point for electrons satisfying the isolation criteria is about 70% for a p_{T} of 20 GeV and reaches a plateau of 95% at a p_{T} of 100 GeV. The corresponding rejection factor for leptons from the decay of b-hadrons is about 50, estimated from a simulated $t\bar{t}$ sample. Correction factors are applied to simulated electrons to take into account the small differences in trigger, reconstruction, identification and isolation efficiencies between data and MC simulation.

Muon candidates are reconstructed by combining a reconstructed track from the inner detector with one from the muon spectrometer, and are required to have $p_{\mathrm{T}} > 15\,\mathrm{GeV}$ and $|\eta| < 2.5$ and to meet the "Medium" identification [83] criteria. Similarly to electrons, muon candidates must have $|d_0|/\sigma(d_0) < 3$ and $|z_0 \sin(\theta)| < 0.5\,\mathrm{mm}$. To reject misidentified muon candidates, several quality requirements are imposed on the muon candidate. An isolation requirement based on ID tracks is imposed, and a threshold is set for the nonprompt-lepton BDT output. The efficiency at the chosen working point for muons satisfying the isolation criteria is about 80% for a p_{T} of 20 GeV and reaches a plateau of 99% at a p_{T} of 100 GeV. The corresponding rejection factor for leptons from the decay of b-hadrons is about 20, estimated from a simulated $t\bar{t}$ sample. Like for electrons, correction factors are applied to simulated muons to account for the small differences between data and simulation.

Jets are reconstructed from the particle-flow objects [84] using the anti-k_t algorithm [85, 86] with the radius parameter set to $R = 0.4$. Their calibration follows the methodology described in Ref. [87]. Jets are required to have $p_{\mathrm{T}} > 25\,\mathrm{GeV}$ and $|\eta| < 2.5$. To suppress jets arising from pileup, a discriminant called the "jet vertex tagger" (JVT) is constructed using a two-dimensional likelihood method [88]. The jet energy scale and resolution are corrected with η- and p_{T}-dependent scale factors.

To identify jets containing a b-hadron (b-jets), the "DL1r" multivariate algorithm is employed [89]. It uses impact parameter and secondary and tertiary vertex information from tracks contained in the jet as input. Operating points are defined by a threshold value for the b-tagging discriminant output and are chosen

to provide a specific b-jet efficiency in an inclusive $t\bar{t}$ sample. Candidate b-jets must have a b-tagging discriminant value that exceeds a threshold corresponding to a 70% b-jet selection efficiency. With this criterion, 0.25% of light-jets, containing neither a b- nor a c-hadron, are misidentified as b-jets, as are 10% of jets initiated by c-quarks. Correction factors are derived and applied to correct for differences in b-jet selection efficiency and the mistagging rates between data and MC simulation [89].

The missing transverse momentum, with magnitude $E_{\mathrm{T}}^{\mathrm{miss}}$, is calculated as the negative of the vector sum of the transverse momenta of all reconstructed objects. To account for soft hadronic activity, a term including tracks associated with the primary vertex but not with any of the reconstructed objects is added to the $E_{\mathrm{T}}^{\mathrm{miss}}$ calculation [90, 91].

To avoid cases where the detector response to a single physical object is reconstructed as two separate final-state objects, an overlap removal procedure is used. If electron and muon candidates share a track, the electron candidate is removed. After that, if the $\Delta R_{y,\phi}$ distance[4] between a jet and an electron candidate is less than 0.2, the jet is discarded. If multiple jets satisfy this requirement, only the closest jet is removed. For jet–electron distances between 0.2 and 0.4, the electron candidate is removed. If the distance between a jet and a muon candidate is less than 0.2, and the jet has less than three associated tracks, the jet is removed. Any muon subsequently found at a distance of less than 0.4 from a jet is removed.

5 Event reconstruction and selection

The analysis searches for effects of FCNC tZq couplings both in $t\bar{t}$ decay and in single-top-quark production processes. In the first process, one of the top quarks decays through the dominant mode into a W boson and a b-quark (hereafter called the "SM top quark", denoted by t_{SM}), while the other top quark (hereafter called the "FCNC top quark", denoted by t_{FCNC}) decays into a Z boson and a u- or c-quark. In the second process, the production of a single top quark proceeds through an FCNC interaction in association with a Z boson, while its decay is through the dominant mode. In each channel, only the trilepton final state is targeted, in which the Z and W bosons decay leptonically. Therefore, the final state of the FCNC process in $t\bar{t}$ decays is characterized by the presence of three leptons, at least two jets, one of which is a b-jet, and missing transverse momentum from the escaping neutrino. The final state of the FCNC process in single top-quark production is instead characterized by the presence of three leptons, a b-jet, up to one additional jet, and missing transverse momentum. Due to the different final states, two separate signal regions (SRs) are defined, targeting the two processes: SR1 targets FCNC processes in $t\bar{t}$ decays while SR2 targets FCNC processes in single top-quark production. The SRs share common selections for the leptons and they differ in their top-quark reconstruction and jet multiplicity requirements.

In both SRs, exactly three leptons (electrons or muons) that do not all have the same charge are required. One of the leptons must have $p_{\mathrm{T}} > 27\,\mathrm{GeV}$, because of the trigger thresholds, and must be matched, with $\Delta R < 0.15$, to the lepton reconstructed by the trigger. Events with a fourth reconstructed lepton are vetoed. At least one opposite-sign same-flavor lepton pair (OSSF) with an invariant mass in the range $|m_{\ell\ell} - 91.2\,\mathrm{GeV}| < 15\,\mathrm{GeV}$ is required. In the μee and $e\mu\mu$ channels the pair is uniquely identified, whereas in the eee and $\mu\mu\mu$ channels both of the possible combinations are considered and the pair with the invariant mass closer to the Z boson mass is chosen. The lepton not used to reconstruct the Z boson is

[4] $\Delta R_{y,\phi}$ is the Lorentz-invariant distance in the rapidity–azimuthal-angle plane, defined as $\Delta R_{y,\phi} = \sqrt{(\Delta y)^2 + (\Delta\phi)^2}$, where y is the rapidity, defined as $y = (1/2)\ln[(E + p_z)/(E - p_z)]$.

assumed to be the one coming from the W boson, ℓ_W. In SR2, to help reject background sources with a third nonprompt lepton, events are required to have $m_{\mathrm{T}}(\ell_W, \nu) > 40\,\mathrm{GeV}$.[5]

In SR1 the selected events have at least two jets, with exactly one b-tagged. In SR2 the selected events have one or two jets, with exactly one b-tagged. For events with exactly two jets, orthogonality between SR1 and SR2 is ensured by using an invariant mass cut on reconstructed top-quark candidates. An additional SR targeting the FCNC tZc coupling in $t\bar{t}$ decay, based on the presence of a c-jet, was considered. The c-tagging was done using the soft-muon tagging technique employed in Ref. [92]. With the current dataset, this SR was found to bring only marginal improvements to the final limits.

In the events having at least two jets with one of them being b-tagged, the reconstruction of FCNC and SM top-quark candidates is based on the "FCNC-in-$t\bar{t}$-decay" signal hypothesis. The kinematics of the top-quark candidates are reconstructed from the corresponding decay particles by minimizing the following expression:

$$\chi^2_{t\bar{t}} = \frac{\left(m^{\mathrm{reco}}_{j_a\ell\ell} - m_{t_{\mathrm{FCNC}}}\right)^2}{\sigma^2_{t_{\mathrm{FCNC}}}} + \frac{\left(m^{\mathrm{reco}}_{j_b\ell_W\nu} - m_{t_{\mathrm{SM}}}\right)^2}{\sigma^2_{t_{\mathrm{SM}}}} + \frac{\left(m^{\mathrm{reco}}_{\ell_W\nu} - m_W\right)^2}{\sigma^2_W}, \tag{2}$$

where $m^{\mathrm{reco}}_{j_a\ell\ell}$, $m^{\mathrm{reco}}_{j_b\ell_W\nu}$, and $m^{\mathrm{reco}}_{\ell_W\nu}$ are the reconstructed masses of the Zq, Wb, and $\ell_W\nu$ systems, respectively. The minimization has two independent parts. The first is the jet permutation, where any non-b-tagged jet can be assigned to j_a, while j_b must correspond to a b-tagged jet. The second is the minimization of the $\chi^2_{t\bar{t}}$ for each permutation by varying the longitudinal component of the neutrino momentum, p^{ν}_z, to determine the most probable value while its transverse component is set to the missing transverse momentum in the event.

This procedure assigns a reconstructed jet to the q-quark from the decay of the FCNC top quark and determines the p^{ν}_z value to reconstruct the four-momenta of the two top-quark candidates.

In Eq. (2), the central values ($m_{t_{\mathrm{FCNC}}}$, $m_{t_{\mathrm{SM}}}$ and m_W) and the widths ($\sigma_{t_{\mathrm{FCNC}}}$, $\sigma_{t_{\mathrm{SM}}}$ and σ_W) of the distributions of the reconstructed masses of the top quark and W boson candidates are taken from reconstructed simulated FCNC-in-$t\bar{t}$-decay signal events that undergo the common object selection procedure just described. This is done by matching the true q- and b-quarks in the simulated events to the reconstructed jets, setting the longitudinal momentum of the neutrino to the p_z of the true generated neutrino, and the transverse component to the missing transverse momentum in the event, and then performing a likelihood fit with a Bukin function[6] [93] to the masses of the reconstructed top quarks and W boson. The mass values for the LH coupling are reported in Table 1. Compatible mass values are obtained for the RH coupling. The fraction of reconstructed top-quark candidates that are matched to the true simulated particles within a cone of size $\Delta R = 0.4$ is $\epsilon_{t_{\mathrm{FCNC}}} = 75\%$ for the FCNC top-quark candidates and $\epsilon_{t_{\mathrm{SM}}} = 54\%$ for the SM top-quark candidates, where the difference comes from the fact that for the SM top-quark decay the match of the missing transverse momentum with the generated neutrino is less efficient.

[5] The transverse mass is calculated using the momentum of the lepton associated with the W boson, the $E^{\mathrm{miss}}_{\mathrm{T}}$ and the azimuthal angle, ϕ, between them: $m_{\mathrm{T}}(\ell_W, \nu) = \sqrt{2p^{\ell}_{\mathrm{T}}E^{\mathrm{miss}}_{\mathrm{T}}\,(1 - \cos\Delta\phi)}$.

[6] These fits use a generalization of the Gaussian function to allow for asymmetric tails in the distribution. The overall normalization is fixed to the yield and the shape of the function is determined by five parameters: the peak position, the width of the core, the asymmetry, the size of the lower tail, and the size of the higher tail. From these parameters, only the peak position and the width enter the χ^2.

Table 1: Summary of the mean values and standard deviations of the invariant mass distributions for the top-quark candidates and the W boson. These values are obtained from the Bukin fits using the FCNC-in-$t\bar{t}$-decay signal samples with the LH coupling. The two FCNC tZu and tZc coupling samples are combined.

	FCNC top quark		SM top quark		W boson	
	$m_{t_{\text{FCNC}}}$ [GeV]	$\sigma_{t_{\text{FCNC}}}$ [GeV]	$m_{t_{\text{SM}}}$ [GeV]	$\sigma_{t_{\text{SM}}}$ [GeV]	m_W [GeV]	σ_W [GeV]
FCNC in $t\bar{t}$ decay (LH)	171.0	11.1	166.5	23.2	80.5	15.4

Under the FCNC-in-single-top-quark-production signal hypothesis, the SM top-quark candidate is instead reconstructed in events having one or two jets, with exactly one b-tagged. The missing transverse momentum is assumed to be the transverse component of the neutrino momentum, while the most probable value of p_z^ν is determined by minimizing the following expression:

$$\chi^2_{tZ} = \frac{\left(m^{\text{reco}}_{j_b\ell_W\nu} - m_{t_{\text{SM}}}\right)^2}{\sigma^2_{t_{\text{SM}}}} + \frac{\left(m^{\text{reco}}_{\ell_W\nu} - m_W\right)^2}{\sigma^2_W}, \tag{3}$$

where $m^{\text{reco}}_{j_b\ell_W\nu}$ and $m^{\text{reco}}_{\ell_W\nu}$ are the reconstructed masses of the Wb and $\ell_W\nu$ systems, respectively. In Eq. (3), the central values for the masses and widths of the top quark and W boson are taken from reconstructed simulated FCNC-in-$t\bar{t}$-decay signal events, as is done in Eq. (2).[7] Therefore, in the events with two jets, the four-momentum of the SM top-quark candidate reconstructed under the FCNC-in-single-top-quark-production signal hypothesis is the same as that reconstructed under the FCNC-in-$t\bar{t}$-decay signal hypothesis. In this case, the fraction of reconstructed top-quark candidates that are matched to the true simulated particles within a cone of size $\Delta R = 0.4$ is $\epsilon_{t_{\text{SM}}} = 71\%$.

In SR1, the mass of the FCNC top-quark candidate, $m^{\text{reco}}_{j_a\ell\ell}$, is required to be within $2\sigma_{t_{\text{FCNC}}}$ of 172.5 GeV, while no requirement is placed on the mass of the SM top-quark candidate, $m^{\text{reco}}_{j_b\ell_W\nu}$. In SR2, the mass of the SM top-quark candidate is required to be within $2\sigma_{t_{\text{SM}}}$ of 172.5 GeV. In addition, to ensure orthogonality with SR1, for events with exactly two jets the mass of the FCNC top-quark candidate is required to be more than $2\sigma_{t_{\text{FCNC}}}$ from 172.5 GeV. Table 2 summarizes the selection criteria applied to the signal regions considered. With these criteria, 496 data events are selected in SR1 and 460 are selected in SR2.

Figure 2 shows the distributions of the masses of the two top-quark candidates in SR1, and the mass of the top-quark candidate and the p_{T} of the reconstructed Z boson in SR2. These kinematic distributions are some of the key features that distinguish signal events from the backgrounds and they are utilized in the multivariate analysis described in Section 6. In SR1, the dominant signal is the FCNC-in-$t\bar{t}$-decay events (shown with solid lines in Figure 2 separately for the tZu and tZc couplings), while the FCNC-in-single-top-quark-production contribution (shown with dashed lines) is smaller. In contrast, SR2 is more sensitive to the tZu FCNC-in-single-top-quark-production signal, with similar smaller contributions from the other three signals. After the event selection the main background sources are $t\bar{t}Z$, tZ and diboson production.

[7] Using the central values for the masses and widths extracted from the FCNC single-top production signal sample does not have a significant effect on the final results.

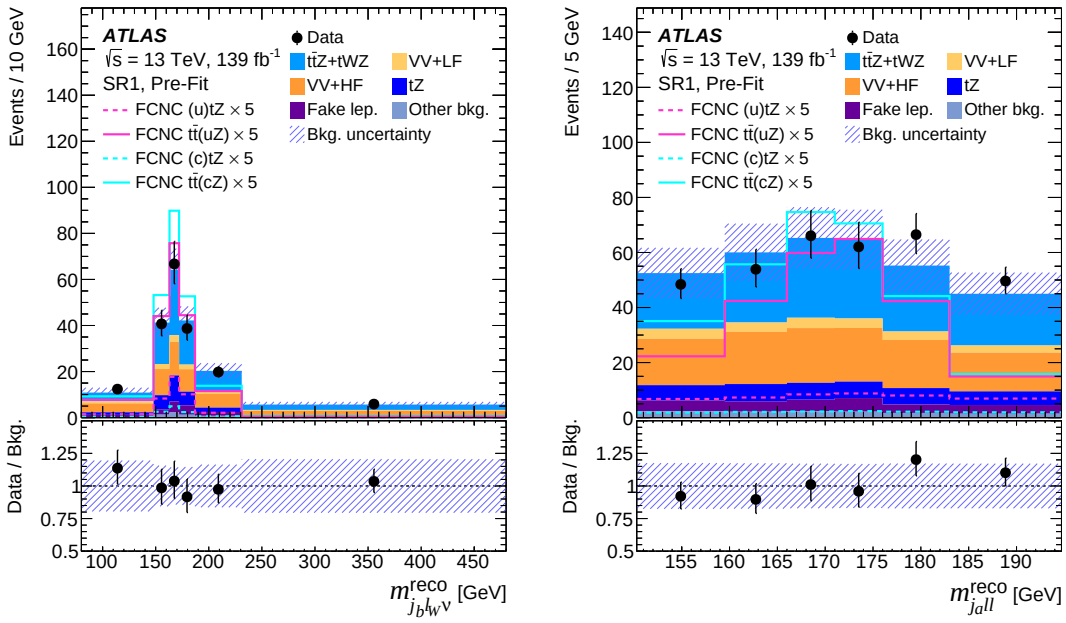

(a) (b)

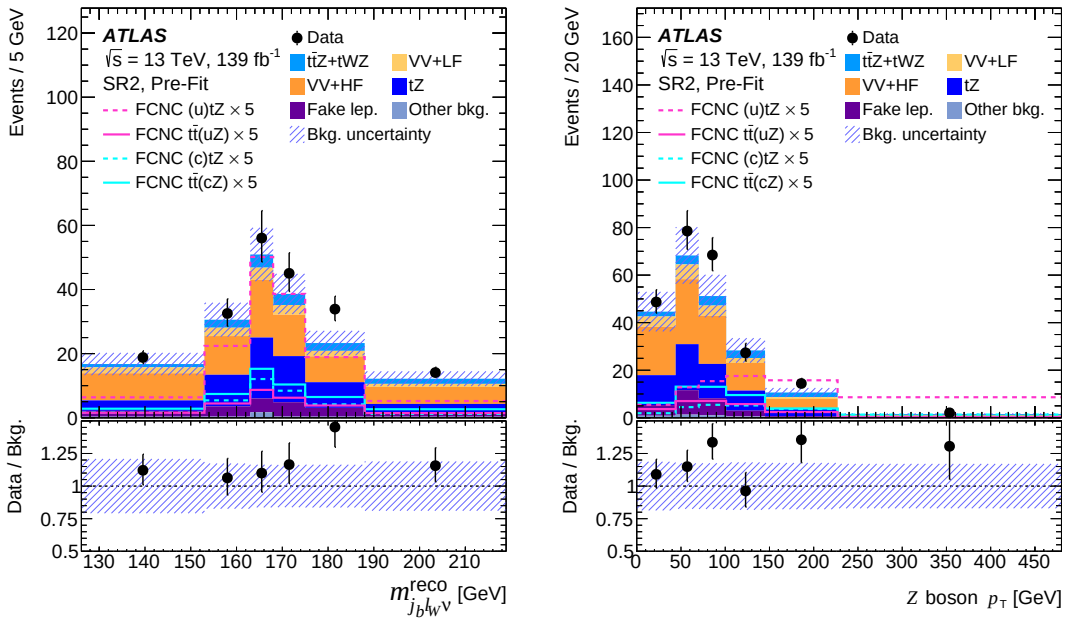

(c) (d)

Figure 2: Comparison between data and background prediction before the fit ("Pre-Fit") for some kinematic distributions in the SRs. The distributions are: (a) the mass of the SM top-quark candidate in SR1, (b) the mass of the FCNC top-quark candidate in SR1, (c) the mass of the SM top-quark candidate in SR2 and (d) the transverse momentum of the Z boson candidate in SR2. The uncertainty band includes both the statistical and systematic uncertainties in the background prediction. The four FCNC LH signals are also shown separately, normalized to five times the cross-section corresponding to the most stringent observed branching ratio limits [21]. The first (last) bin in all distributions includes the underflow (overflow). The lower panels show the ratios of the data ("Data") to the background prediction ("Bkg.").

Table 2: Overview of the requirements applied to select the events in the signal regions. OSSF is an opposite-sign same-flavor lepton pair, $m_Z = 91.2\,\text{GeV}$ and $m_t = 172.5\,\text{GeV}$.

Common selections		
Exactly 3 leptons with $p_{\text{T}}(\ell_1) > 27\,\text{GeV}$ ≥ 1 OSSF pair, with $\lvert m_{\ell\ell} - m_Z \rvert < 15\,\text{GeV}$		
SR1	SR2	
≥ 2 jets	1 jet	2 jets
1 b-jet	1 b-jet	1 b-jet
–	$m_{\text{T}}(\ell_W, \nu) > 40\,\text{GeV}$	$m_{\text{T}}(\ell_W, \nu) > 40\,\text{GeV}$
$\lvert m^{\text{reco}}_{j_a \ell\ell} - m_t \rvert < 2\sigma_{t_{\text{FCNC}}}$	–	$\lvert m^{\text{reco}}_{j_a \ell\ell} - m_t \rvert > 2\sigma_{t_{\text{FCNC}}}$
–	$\lvert m^{\text{reco}}_{j_b \ell_W \nu} - m_t \rvert < 2\sigma_{t_{\text{SM}}}$	$\lvert m^{\text{reco}}_{j_b \ell_W \nu} - m_t \rvert < 2\sigma_{t_{\text{SM}}}$

6 Background estimation and separation from signal

Two classes of backgrounds are considered: processes in which three or more prompt leptons are produced, such as diboson production or the associated production of top quarks ($t\bar{t}Z$, tWZ, tZ, $t\bar{t}W$, $t\bar{t}H$) and processes with two prompt leptons in the final state along with one additional nonprompt or fake lepton that satisfies the selection criteria, such as $t\bar{t}$, tW, and Z + jets. Such nonprompt or fake leptons can originate from decays of bottom or charm hadrons, jets misidentified as electrons, leptons from kaon or pion decays, or electrons from photon conversions.

All background contributions are estimated by using MC samples that are normalized to their respective SM predicted cross-sections calculated at NLO in QCD. The cross-section of the $t\bar{t}H$ background includes NLO+NLL soft-gluon resummation [94]. For the $t\bar{t} + tW$ nonprompt lepton backgrounds the normalization is extracted from data, as described later.

After applying the event selection requirements, diboson, $t\bar{t}Z$ and tZ production constitute the largest backgrounds. For SR1, the dominant backgrounds are $t\bar{t}Z$ and VV + HF production. Monte Carlo simulation indicates that these represent more than 65% of the total number of selected background events in this region, with the two processes contributing equally. For SR2, VV + HF and tZ are the dominant backgrounds, giving 70% of background events. The processes with nonprompt leptons constitute a minor background, with their contribution being at most 10% of the total selected events.

Four control regions (CRs) are defined and used in the fit that is described in Section 8. The CRs are used to adjust the normalization and to reduce the associated systematic uncertainties in the main backgrounds. The selections applied to define the CRs are summarized in Table 3 and described in the following.

A $t\bar{t}$ CR is designed to control the $t\bar{t}$ background. The $t\bar{t}$ CR is constructed by requiring the presence of three leptons, with one of the possible pairs having opposite charge, as in the SRs. To veto the presence of a Z boson, the opposite-sign lepton pair is also required to consist of different flavors. Events with at least one jet, with exactly one b-tagged, are considered. This region is dominated by $t\bar{t}$ events with 40% contamination from other backgrounds, mainly $t\bar{t}W$ and $t\bar{t}H$. A total of 157 data events are selected for the $t\bar{t}$ CR.

To control the $t\bar{t}Z$ background, a $t\bar{t}Z$ CR is defined. The requirements on the leptons are the same as for the SRs, while at least four jets, with exactly two b-tagged, are required. This region is dominated by $t\bar{t}Z$

events with 25% contamination from other backgrounds, mainly tZ and VV + HF. A total of 286 data events are selected for the $t\bar{t}Z$ CR.

Two mass sideband CRs are also included. These CRs are designed to contain a mixture of the main background sources ($t\bar{t}Z$ and diboson). The mass sideband CR1 is defined with almost the same event selection as SR1, with the differences being that the mass of the FCNC top-quark candidate must be more than $2\sigma_{t_{\text{FCNC}}}$ from 172.5 GeV, and the mass of the SM top-quark candidate must also be more than $2\sigma_{t_{\text{SM}}}$ from 172.5 GeV. The mass sideband CR2 is defined with almost the same event selection as SR2, with the differences being that only events with one jet are considered and that the mass of the SM top-quark candidate must be more than $2\sigma_{t_{\text{SM}}}$ from 172.5 GeV. Totals of 343 and 104 data events are selected for the mass sidebands CR1 and CR2 respectively.

Table 3: Overview of the requirements applied to select the events in the control regions. OSSF is an opposite-sign same-flavor lepton pair, m_Z = 91.2 GeV and m_t = 172.5 GeV.

Common selections			
Exactly 3 leptons with $p_{\text{T}}(\ell_1) > 27$ GeV			
$t\bar{t}$ CR	$t\bar{t}Z$ CR	Sideband CR1	Sideband CR2
≥ 1 OS pair, no OSSF	≥ 1 OSSF pair with $\lvert m_{\ell\ell} - m_Z \rvert < 15$ GeV	≥ 1 OSSF pair with $\lvert m_{\ell\ell} - m_Z \rvert < 15$ GeV	≥ 1 OSSF pair with $\lvert m_{\ell\ell} - m_Z \rvert < 15$ GeV
–	–	–	$m_{\text{T}}(\ell_W, \nu) > 40$ GeV
≥ 1 jet	≥ 4 jets	≥ 2 jets	1 jet
1 b-jet	2 b-jets	1 b-jet	1 b-jet
–	–	$\lvert m^{\text{reco}}_{j_a\ell\ell} - m_t \rvert > 2\sigma_{t_{\text{FCNC}}}$	–
–	–	$\lvert m^{\text{reco}}_{j_b\ell_W\nu} - m_t \rvert > 2\sigma_{t_{\text{SM}}}$	$\lvert m^{\text{reco}}_{j_b\ell_W\nu} - m_t \rvert > 2\sigma_{t_{\text{SM}}}$

To better separate the signal from the backgrounds, a multivariate analysis (MVA) technique is used. The chosen MVA is the gradient boosted decision tree (GBDT) method implemented with TMVA [95, 96]. Decision trees [97] recursively partition the parameter space into regions where signal or background purities are enhanced. Gradient boosting is a method which improves the performance and stability of decision trees and involves the combination of many trees into a single final discriminant. After boosting, the final score undergoes a transformation to map the scores onto the interval −1 to +1. The most signal-like events have scores near +1 while the most background-like events have scores near −1. A k-fold cross validation is employed.

The GBDT training is done separately for the LH and RH samples and in each SR as follows. In SR1, for both the FCNC tZu and tZc coupling searches, the expected contribution from FCNC processes in $t\bar{t}$ decay is significantly higher than the one from single-top-quark production. Therefore, the GBDT is trained with only the FCNC-in-$t\bar{t}$-decay signal against all backgrounds. Since the kinematics of FCNC-in-$t\bar{t}$-decay events for tZu and tZc couplings are similar, the FCNC-in-$t\bar{t}$-decay signal samples with the two couplings are combined to train the GBDT. Therefore, in SR1 a single MVA discriminant, D_1, is built for both the FCNC tZu and tZc coupling searches. In contrast, SR2 is particularly sensitive to the FCNC tZu coupling in single-top-production events. Thus, the corresponding MVA discriminant, D_2^u, is built by training the GBDT with the the tZu-coupling FCNC-in-single-top-production sample against all backgrounds. Despite the lower sensitivity to the FCNC tZc coupling in SR2, this region is used in combination with SR1 in the search for a FCNC tZc coupling signal. In the total expected FCNC tZc signal yield, the contribution from the FCNC processes in $t\bar{t}$ decay events is comparable to the one from the single-top-quark-production

events. Therefore, in SR2 the MVA discriminant for the search for a FCNC tZc coupling signal, D_2^c, is built using both the FCNC-in-$t\bar{t}$-decay and FCNC-in-single-top-production samples against all backgrounds.

For the training of each of the three discriminants, a total of six variables is used. These variables are chosen from a larger set. Only variables that provide good separation and are well modeled are used in the final training. For the D_1 discriminant the six variables are: the reconstructed masses of the SM and FCNC top-quark candidates, the ΔR separation between them, the ΔR separation between the lepton from the SM top-quark decay and the reconstructed Z boson, the number of jets, and the transverse momentum of the jets associated with the u/c-quark from the FCNC top-quark candidate's decay. For both the D_2^u and D_2^c discriminants the following six variables are used: the p_{T} of the Z boson and of the b-tagged jet, the ΔR separation between them, the SM top-quark candidate's mass, the ΔR separation between the lepton from the SM top-quark candidate decay and the reconstructed Z boson, and the χ^2 from the kinematic fit under the signal hypothesis of an FCNC process in single-top-quark production.

7 Systematic uncertainties

Systematic uncertainties in the signal acceptance and in the normalization of the individual backgrounds, as well as uncertainties in the shape of the fitted distributions, are taken into account. These are treated as being correlated between the different regions, unless stated otherwise. The uncertainties are classified into the following categories:

Reconstruction efficiency and calibration uncertainties: Systematic uncertainties affecting the reconstruction efficiency and energy calibration of electrons, muons, jets and b-jets are propagated through the analysis.

The differences between the electron (muon) trigger, reconstruction, selection and isolation efficiencies in data and those in MC simulation are corrected for by scale factors derived from dedicated $Z \to e^+e^-$ ($Z \to \mu^+\mu^-$) enriched control samples using a tag-and-probe method [81, 83]. Uncertainties in these scale factors are taken into account. Moreover, uncertainties are included for the electron (muon) energy (momentum) scale and resolution [81, 83].

For the jets, an uncertainty for the JVT requirement is considered. The jet energy scale was derived using information from test-beam data, LHC collision data and simulation, as described in Ref. [98]. The impact of the uncertainty in the jet energy resolution is also evaluated.

The b-tagging efficiencies and mistagging rates are measured in data using the same methods as described in Refs. [99–101], with the systematic uncertainties due to b-tagging efficiency and the mistagging rates calculated separately. The impact of the uncertainties on the b-tagging calibration is evaluated separately for b-, c- and light-jets in the MC samples.

The uncertainty in $E_{\mathrm{T}}^{\mathrm{miss}}$ due to a possible miscalibration of the soft-track component of the $E_{\mathrm{T}}^{\mathrm{miss}}$ is derived from data–MC comparisons of the p_{T} balance between the hard and soft $E_{\mathrm{T}}^{\mathrm{miss}}$ components [90]. The uncertainty associated with the leptons and jets is propagated from the corresponding uncertainties in the energy/momentum scales and resolutions, and is classified together with the uncertainty associated with the corresponding objects.

Signal and background modeling: The systematic uncertainties due to MC modeling of the signal and the main backgrounds are estimated by comparing samples from different MC generators and PDF sets and by varying the parameters associated with the renormalization and factorization scales, and additional radiation. For some processes, some of these uncertainties are found to be negligible and therefore they are not mentioned in the following.

For the signal, the effects of the systematic uncertainty in the renormalization and factorization scales, μ_r and μ_f, are taken into account by varying these parameters by factors of 2 and 0.5 with respect to their default values and comparing the results of these variations with the nominal prediction. The uncertainty in the modeling of the parton shower is estimated by comparing the nominal signal sample with one generated with HERWIG 7 instead of PYTHIA 8. PDF uncertainties are found to be negligible and are not included for the signal.

For the $t\bar{t}Z$ and tZ backgrounds, the following uncertainties are included. The effect of changing the parton shower is considered as an uncertainty, following the same strategy used for the signal. The uncertainty due to ISR is estimated by comparing the nominal event sample with two samples where the Var3c up and down variations of the A14 tune were employed. Uncertainties from the variation of μ_r and μ_f are also included.

For the tWZ background, the effect of changing the modeling of the interference with $t\bar{t}Z$ is included by comparing two different diagram removal predictions.

The effect of changing the MC generator for the modeling of the diboson background is considered as an uncertainty. It is evaluated by comparing the nominal SHERPA sample with one generated with POWHEG BOX. This uncertainty is split into the two light- and heavy-flavor components and evaluated separately for each jet multiplicity. Uncertainties in the μ_r and μ_f scales, as well as in the PDF and in α_s are also included for the diboson background.

For the $t\bar{t}$ background, several sources of uncertainty are taken into account. The effect of changing the parton shower is included as an uncertainty. The Var3c A14 tune variations, as well as variations of μ_r and μ_f are also included. Additionally, the uncertainty associated with the h_{damp} parameter is evaluated by using the alternative sample with the h_{damp} value increased to $3\,m_t$. The NNPDF3.0LO replicas are used to evaluate the PDF uncertainties for the nominal PDF. Finally, an uncertainty is added to take into account the differences in $t\bar{t}$ background composition between the SRs and the $t\bar{t}$ CR, which is used to control the $t\bar{t}$ background in the fit to data. In particular, the fractions of nonprompt leptons originating from each source are computed, separately for photon conversions and b-hadron decays, in the SRs and in the $t\bar{t}$ CR, for each jet multiplicity. Then the maximum variation of the fractions between the control region and the signal regions is taken as an uncertainty.

Signal and background rate uncertainty: The $t\bar{t}$ cross-section uncertainties due to the PDF and α_s are calculated using the PDF4LHC15 prescription [102] with the MSTW2008NNLO [103, 104], CT10NNLO [65, 105] and NNPDF2.3LO PDF sets, and are added in quadrature to the effect of the scale uncertainty, resulting in a total uncertainty of 5.5% that is assigned to the FCNC-in-$t\bar{t}$-decay signal.

For the $t\bar{t}Z$ background, a 12% rate uncertainty is included [106], and for the $t\bar{t}H$ process the normalization uncertainty is 15% [106], while for $t\bar{t}W$ a more conservative 50% is used [107]. For the tZ process, an uncertainty of 15% in the normalization is applied [108, 109], while for the tWZ process a more conservative 30% is used. For VV + LF production, the normalization uncertainty is taken to be 20% [110] and for VV + HF production it is 30% [111]. Concerning the Z + jets process, a rate uncertainty of 100% is

applied, due to the presence of a nonprompt lepton. A conservative overall normalization uncertainty of 50% is applied to the remaining minor backgrounds ($t\bar{t}t$, $t\bar{t}t\bar{t}$, VVV, VH and $t\bar{t}WW$). These background components are typically well below 1% in the SRs.

Luminosity: The uncertainty in the combined 2015–2018 integrated luminosity is 1.7% [112], obtained using the LUCID-2 detector [113] for the primary luminosity measurements.

Uncertainty in pileup modeling: The uncertainty in pileup modeling is accounted for by varying the reweighting of the MC samples to the data pileup conditions, using the uncertainty in the average number of interactions per bunch crossing.

8 Results

A simultaneous binned profile likelihood fit to the data in the SRs and the CRs is performed using MC distributions of both the signal and background predictions. Four separate fits are performed to extract LH and RH results for the FCNC tZu and tZc couplings. Only the relevant signal templates are used in each fit. The templates are binned distributions of the D_1 discriminant in SR1 and in the mass sideband CR1; the D_2^u discriminant in SR2 and in the mass sideband CR2; and the total event yields in the $t\bar{t}$ CR and the $t\bar{t}Z$ CR. When fitting to extract limits on the FCNC tZc coupling, the D_2^c discriminant is used instead of D_2^u.

The fitted SRs are defined from the SRs described in Section 5 after removing events that constitute two validation regions (VRs) that are not included in the fit, but the fit results are propagated to those regions. The VRs are used to check the stability of the fit and they are obtained by applying a selection on the GBDT discriminants. VR1 is defined by selecting events with $D_1 < -0.6$ from the SR1, while VR2 contains events from SR2 with $D_2^u < -0.7$ and $D_2^c < -0.4$. With the given normalization of the signal samples, the fraction of signal events that is selected from the SRs to enter the VRs ranges from 2% to 5%, depending on the SR. The signal contamination in the VRs is at most 2%. The signal selection efficiency for the FCNC-in-$t\bar{t}$-decay signal in SR1 ranges between 4% and 5%, while that for the FCNC-in-single-top-production signal in SR2 ranges between 3% and 4%. In contrast, the signal selection efficiency for the FCNC-in-$t\bar{t}$-decay signal in SR2 and the FCNC-in-single-top-production signal in SR1 is around 1%.

The statistical analysis used to extract the signal is based on a binned likelihood function $\mathcal{L}(\mu, \vec{\theta})$ constructed as a product of Poisson probability terms over all bins in each considered distribution, and Gaussian constraint terms for $\vec{\theta}$, a set of nuisance parameters that parameterize effects of MC statistical and systematic uncertainties in the signal and background expectations. The signal strength parameter μ is a multiplicative factor applied to the number of signal events normalized to a reference branching ratio. For that, the most stringent limits mentioned in Section 1 are used. The nuisance parameters are allowed to vary in the combined fit to adjust the expectations for signal and background according to the corresponding systematic uncertainties, and their final values are the adjustment that best fits the data. The normalization of the $t\bar{t} + tW$ backgrounds is unconstrained in the fit.

A test statistic, $\tilde{q}_\mu$, is constructed according to the profile likelihood ratio:

$$\tilde{q}_\mu = \begin{cases} -2\ln\left(\dfrac{\mathcal{L}\left(\mu, \hat{\hat{\theta}}(\mu)\right)}{\mathcal{L}\left(0, \hat{\hat{\theta}}(0)\right)}\right) & \text{if } \hat{\mu} < 0, \\ -2\ln\left(\dfrac{\mathcal{L}\left(\mu, \hat{\hat{\theta}}(\mu)\right)}{\mathcal{L}\left(\hat{\mu}, \hat{\theta}\right)}\right) & \text{if } 0 \leq \hat{\mu} \leq \mu, \\ 0 & \text{if } \hat{\mu} > \mu, \end{cases} \tag{4}$$

where $\hat{\mu}$ and $\hat{\theta}$ are the parameters that maximize the likelihood, and $\hat{\hat{\theta}}$ are the nuisance parameter values that maximize the likelihood for a given μ hypothesis. This test statistic is used to determine the probability for accepting the background-only hypothesis for the observed data.

Table 4 shows the pre- and post-fit predictions for the signal and background event yields along with the observed numbers of events in the VRs. The post-fit yields refer to the fit for the FCNC tZu LH coupling extraction. The data and background expectation are in better agreement after the fit, with an increase of the VV + HF background normalization within its pre-fit uncertainty. The post-fit level of agreement between data and the background prediction in the VRs shows no significant mismodeling.

Table 4: Predicted and observed yields in the two VRs considered in the fit. The signal and background predictions are shown before ("Pre-fit") and after the fit to data for the FCNC tZu LH coupling extraction ("Post-fit"). The quoted uncertainties include the statistical and systematic uncertainties of the yields. For the post-fit predictions, they are computed taking into account correlations among nuisance parameters and among processes. For the backgrounds with a nonprompt or fake lepton, the contribution from $t\bar{t}$ + tW is shown separately from "Other fakes". For the minor backgrounds, the contribution from $t\bar{t}W$ and $t\bar{t}H$ are shown separately from "Other bkg.".

	Pre-fit		Post-fit	
	VR1	VR2	VR1	VR2
$t\bar{t}Z + tWZ$	70 ± 10	2.2 ± 0.6	70 ± 7	2.4 ± 0.6
VV + LF	10 ± 5	9.8 ± 3.4	10 ± 5	9.7 ± 3.0
VV + HF	56 ± 28	36 ± 14	60 ± 14	47 ± 8
tZ	6.5 ± 1.6	13.5 ± 2.7	6.6 ± 1.5	14.7 ± 2.6
$t\bar{t}$ + tW fakes	5.4 ± 2.6	4.5 ± 1.7	4.8 ± 2.1	3.8 ± 1.4
Other fakes	0.0 ± 0.6	1.4 ± 1.9	0.03 ± 0.24	0.8 ± 1.1
$t\bar{t}W$	2.3 ± 1.2	0.48 ± 0.26	2.3 ± 1.2	0.48 ± 0.25
$t\bar{t}H$	3.0 ± 0.5	0.101 ± 0.032	3.0 ± 0.5	0.108 ± 0.033
Other bkg.	0.8 ± 0.4	0.5 ± 0.7	0.8 ± 0.4	0.5 ± 0.6
Total background	154 ± 31	69 ± 15	158 ± 13	79 ± 7
Data	151	80	151	80
Data / Bkg.	0.98 ± 0.22	1.16 ± 0.29	0.96 ± 0.11	1.01 ± 0.15

Tables 5 and 6 show the observed number of events in data and the post-fit predictions for the signal and background event yields in the SRs and CRs. The yields refer to the fit for the FCNC tZu LH coupling extraction. Good agreement between data and the SM expectation is observed. The normalization factor for the $t\bar{t} + tW$ backgrounds, which is an unconstrained fit parameter, agrees with unity within uncertainties. The variations of the post-fit background normalizations are within pre-fit uncertainties. All post-fit values of the nuisance parameters are less than one standard deviation from the pre-fit values. The statistical component is the dominant contribution in the total uncertainty. The same conclusions are obtained from the fits for the other FCNC couplings.

Table 5: Predicted and observed yields in the two SRs considered in the fit. The signal and background predictions are shown after the fit to data for the FCNC tZu LH coupling extraction. The quoted uncertainties include the statistical and systematic uncertainties of the yields, computed taking into account correlations among nuisance parameters and among processes. For the backgrounds with a nonprompt or fake lepton, the contribution from $t\bar{t} + tW$ is shown separately from "Other fakes". For the minor backgrounds, the contribution from $t\bar{t}W$ and $t\bar{t}H$ are shown separately from "Other bkg.".

	SR1 ($D_1 > -0.6$)	SR2 ($D_2^u > -0.7$ or $D_2^c > -0.4$)
$t\bar{t}Z + tWZ$	137 ± 12	36 ± 6
VV + LF	18 ± 7	24 ± 8
VV + HF	114 ± 19	162 ± 26
tZ	46 ± 7	108 ± 18
$t\bar{t} + tW$ fakes	14 ± 4	27 ± 8
Other fakes	7 ± 8	5 ± 6
$t\bar{t}W$	4.2 ± 2.1	3.1 ± 1.6
$t\bar{t}H$	4.8 ± 0.7	0.89 ± 0.17
Other bkg.	2.0 ± 1.0	2.5 ± 2.9
FCNC $(u)tZ$	0.9 ± 1.7	4 ± 8
FCNC $t\bar{t}(uZ)$	5 ± 9	0.8 ± 1.5
Total background	348 ± 15	369 ± 21
Data	345	380

Table 6: Predicted and observed yields in the four CRs considered in the fit. The signal and background predictions are shown after the fit to data for the FCNC tZu LH coupling extraction. The quoted uncertainties include the statistical and systematic uncertainties of the yields, computed taking into account correlations among nuisance parameters and among processes. For the backgrounds with a nonprompt or fake lepton, the contribution from $t\bar{t} + tW$ is shown separately from "Other fakes". For the minor backgrounds, the contribution from $t\bar{t}W$ and $t\bar{t}H$ are shown separately from "Other bkg.".

	Sideband CR1	Sideband CR2	$t\bar{t}Z$ CR	$t\bar{t}$ CR
$t\bar{t}Z + tWZ$	102 ± 14	8.2 ± 1.4	230 ± 18	15.4 ± 1.5
VV + LF	27 ± 11	12 ± 4	0.23 ± 0.19	0.38 ± 0.25
VV + HF	166 ± 25	64 ± 9	17 ± 8	2.9 ± 0.5
tZ	22 ± 4	6.8 ± 1.4	21 ± 5	0.96 ± 0.19
$t\bar{t} + tW$ fakes	9.3 ± 2.6	7.2 ± 2.1	4.0 ± 1.3	93 ± 19
Other fakes	2 ± 4	2.0 ± 2.8	0.15 ± 0.18	0.08 ± 0.09
$t\bar{t}W$	4.5 ± 2.3	2.3 ± 1.2	3.0 ± 1.5	27 ± 13
$t\bar{t}H$	2.6 ± 0.4	0.33 ± 0.07	7.5 ± 1.2	14.1 ± 2.2
Other bkg.	3.3 ± 2.5	0.8 ± 0.4	1.9 ± 0.9	3.2 ± 1.5
FCNC $(u)tZ$	0.4 ± 0.7	0.17 ± 0.33	0.09 ± 0.18	0.05 ± 0.10
FCNC $t\bar{t}(uZ)$	0.14 ± 0.27	0.04 ± 0.07	0.11 ± 0.20	0.018 ± 0.035
Total background	338 ± 18	104 ± 8	284 ± 16	157 ± 13
Data	343	104	286	157

The μ parameters are shown in Table 7.

Table 7: Summary of the signal strength μ parameters obtained from the fits to extract LH and RH results for the FCNC tZu and tZc couplings. For the reference branching ratio, the most stringent limits are used [21].

Vertex	Coupling	μ
tZu	LH	0.08 ± 0.12 (stat.) ± 0.08 (syst.)
tZu	RH	0.10 ± 0.12 (stat.) ± 0.08 (syst.)
tZc	LH	0.10 ± 0.17 (stat.) ± 0.14 (syst.)
tZc	RH	0.06 ± 0.16 (stat.) ± 0.13 (syst.)

Figure 3 shows the distributions of the fitted variables in the CRs and SRs after the fit for the FCNC tZu LH coupling extraction. For the FCNC tZc LH coupling extraction, the fitted distributions are presented in Figure 4, where D_2^c is used in SR2 and in the mass sideband CR2. For the $t\bar{t}$ and $t\bar{t}Z$ CRs, only the event yields are used. The data and background prediction agree within the uncertainties.

Limits on each FCNC $t \to Zq$ branching ratio are computed with the CL_s method [114] using the asymptotic properties of q_μ [115] and assuming that only the corresponding FCNC coupling contributes. The observed and expected 95% confidence-level (CL) limits on the branching ratios are shown in Table 8, where the limits on the relevant Wilson coefficients are also reported. The expected limits on the branching ratios calculated without systematic uncertainties are lower by 20% and 25% for the tZu and tZc couplings, respectively. The leading systematic uncertainties include the uncertainty in the SM tZ background normalization and the diboson modeling uncertainties.

Table 8 also shows limits on the FCNC tZu LH and RH couplings obtained when considering only one SR, either SR1 or SR2, and all CRs in the likelihood. The results show that SR2, targeting the FCNC single-top-production signal, contributes more strongly than SR1 to the combined limits. Separate results for the FCNC tZc coupling are not shown, since the limits are dominated by the FCNC-$t\bar{t}$-in-decay signal.

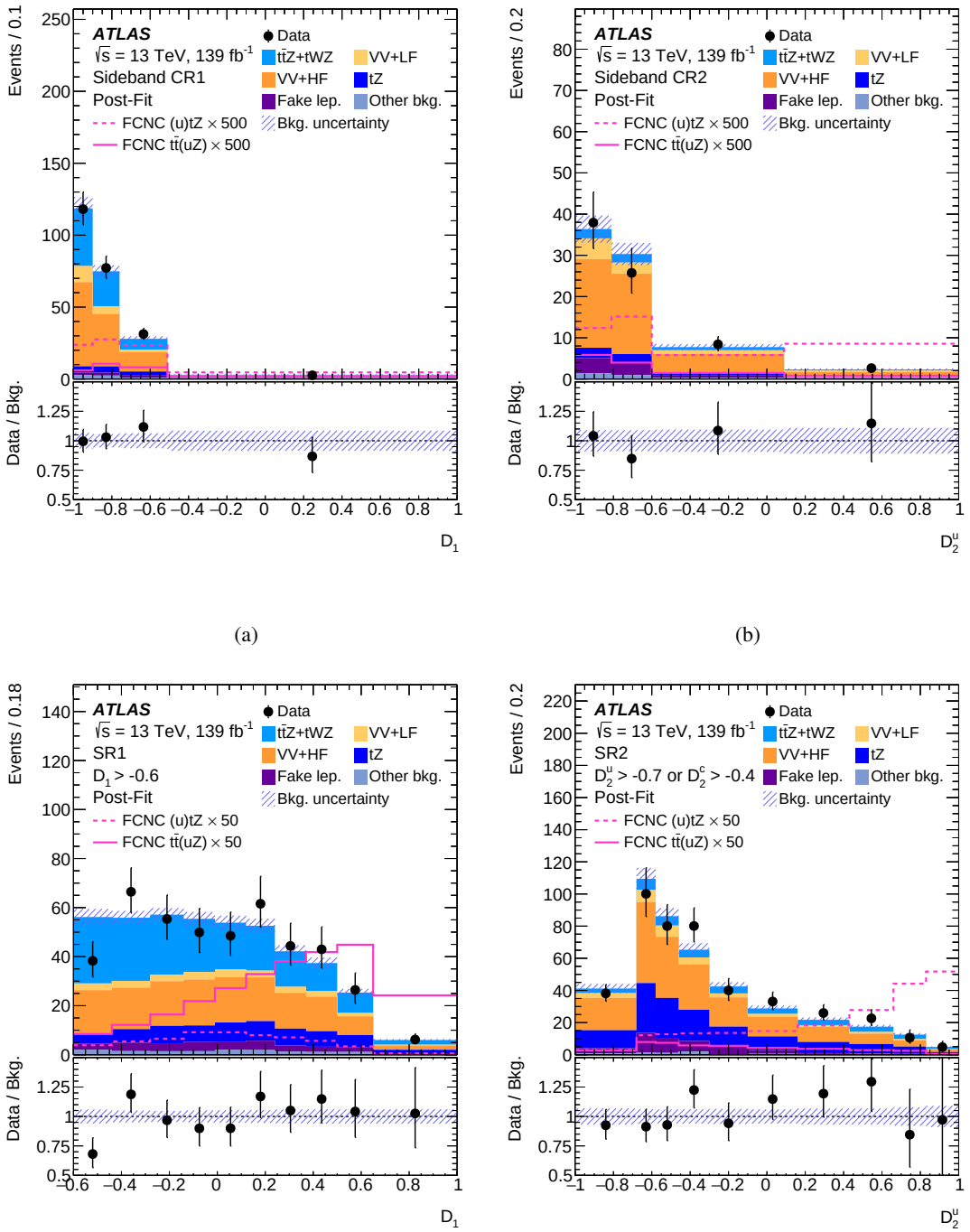

Figure 3: Comparison between data and background prediction after the fit to data ("Post-Fit") for the FCNC tZu LH coupling extraction for the fitted distributions in the CRs and SRs. The distributions are: (a) the D_1 discriminant in the mass sideband CR1, (b) the D_2^u discriminant in the mass sideband CR2, (c) the D_1 discriminant in SR1 and (d) the D_2^u discriminant in SR2. The uncertainty band includes both the statistical and systematic uncertainties in the background prediction. The FCNC tZu LH signals are also separately shown, normalized to 500 or 50 times the best fit of the signal yield. The lower panels show the ratios of the data ("Data") to the background prediction ("Bkg.").

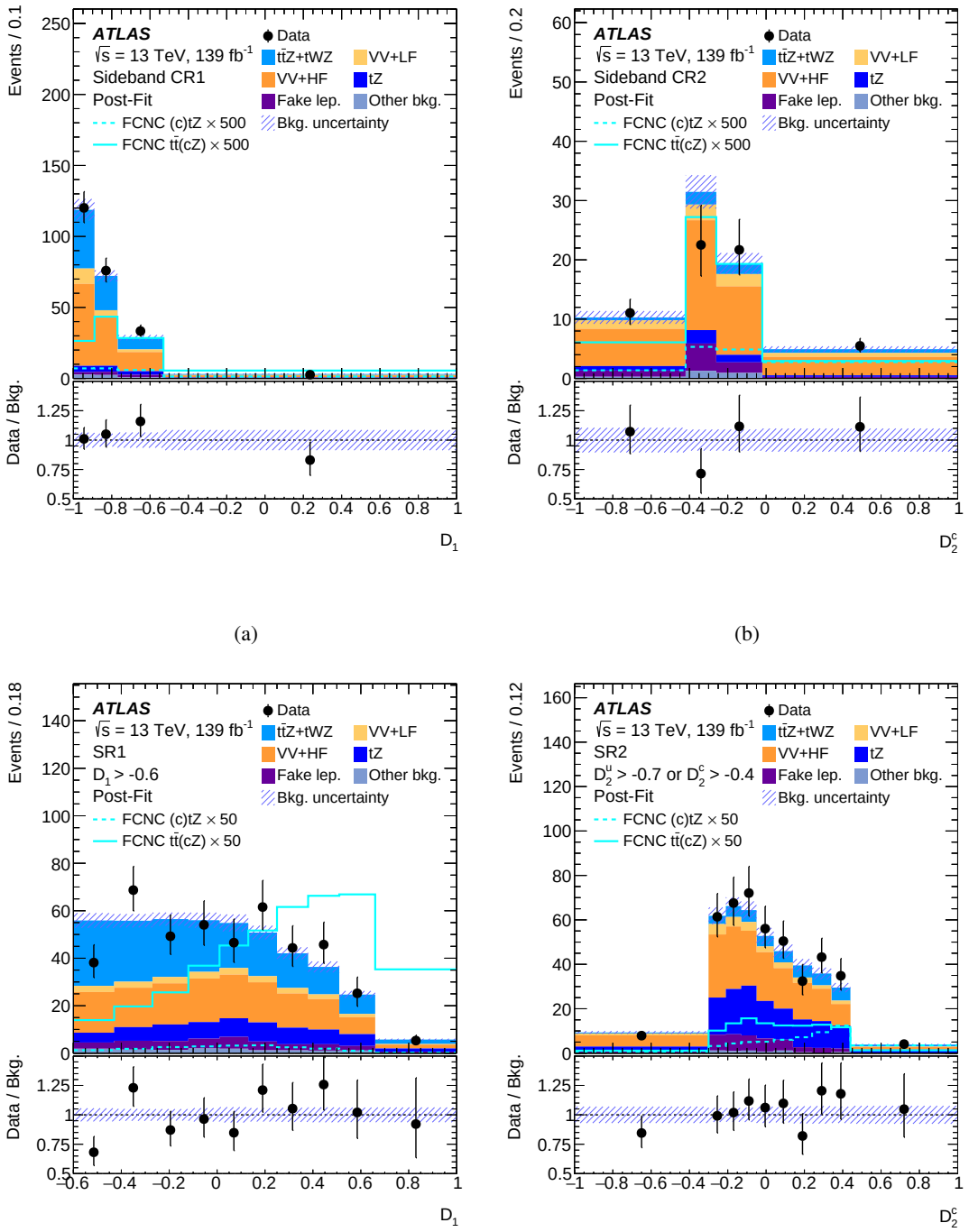

Figure 4: Comparison between data and background prediction after the fit to data ("Post-Fit") for the FCNC tZc LH coupling extraction for the fitted distributions in the CRs and SRs. The distributions are: (a) the D_1 discriminant in the mass sideband CR1, (b) the D_2^c discriminant in the mass sideband CR2, (c) the D_1 discriminant in SR1 and (d) the D_2^c discriminant in SR2. The uncertainty band includes both the statistical and systematic uncertainties in the background prediction. The FCNC tZc LH signals are also separately shown, normalized to 500 or 50 times the best fit of the signal yield. The lower panels show the ratios of the data ("Data") to the background prediction ("Bkg.").

Table 8: Observed and expected 95% CL limits on the FCNC $t \to Zq$ branching ratios and the effective coupling strengths for different vertices and couplings (top eight rows). For the latter, the energy scale is assumed to be $\Lambda_{\text{NP}} = 1$ TeV. The bottom rows show, for the case of the FCNC $t \to Zu$ branching ratio, the observed and expected 95% CL limits when only one of the two SRs, either SR1 or SR2, and all CRs are included in the likelihood.

Observable	Vertex	Coupling	Observed	Expected
	SRs+CRs			
$\mathcal{B}(t \to Zq)$	tZu	LH	6.2×10^{-5}	$4.9\,^{+2.1}_{-1.4} \times 10^{-5}$
$\mathcal{B}(t \to Zq)$	tZu	RH	6.6×10^{-5}	$5.1\,^{+2.1}_{-1.4} \times 10^{-5}$
$\mathcal{B}(t \to Zq)$	tZc	LH	13×10^{-5}	$11\,^{+5}_{-3} \times 10^{-5}$
$\mathcal{B}(t \to Zq)$	tZc	RH	12×10^{-5}	$10\,^{+4}_{-3} \times 10^{-5}$
$\lvert C_{uW}^{(13)*}\rvert$ and $\lvert C_{uB}^{(13)*}\rvert$	tZu	LH	0.15	$0.13\,^{+0.03}_{-0.02}$
$\lvert C_{uW}^{(31)}\rvert$ and $\lvert C_{uB}^{(31)}\rvert$	tZu	RH	0.16	$0.14\,^{+0.03}_{-0.02}$
$\lvert C_{uW}^{(23)*}\rvert$ and $\lvert C_{uB}^{(23)*}\rvert$	tZc	LH	0.22	$0.20\,^{+0.04}_{-0.03}$
$\lvert C_{uW}^{(32)}\rvert$ and $\lvert C_{uB}^{(32)}\rvert$	tZc	RH	0.21	$0.19\,^{+0.04}_{-0.03}$
	SR1+CRs			
$\mathcal{B}(t \to Zq)$	tZu	LH	9.7×10^{-5}	$8.6\,^{+3.6}_{-2.4} \times 10^{-5}$
$\mathcal{B}(t \to Zq)$	tZu	RH	9.5×10^{-5}	$8.2\,^{+3.4}_{-2.3} \times 10^{-5}$
	SR2+CRs			
$\mathcal{B}(t \to Zq)$	tZu	LH	7.8×10^{-5}	$6.1\,^{+2.7}_{-1.7} \times 10^{-5}$
$\mathcal{B}(t \to Zq)$	tZu	RH	9.0×10^{-5}	$6.6\,^{+2.9}_{-1.8} \times 10^{-5}$

9 Conclusions

A search for FCNC processes involving a top quark, an up-type quark and a Z boson is presented. FCNC tZq couplings are searched for both in $t\bar{t}$ decay events, where one top quark decays according to the SM and the other one decays as $t \to Zq$, and in single top-quark production through the $gq \to tZ$ FCNC process, followed by SM top-quark decay. The analysis uses 139 fb^{-1} of pp collision data collected by the ATLAS experiment at the LHC between 2015 and 2018 at a center-of-mass energy of 13 TeV. Events with three leptons, a b-tagged jet, possible additional jets and missing transverse momentum are selected. Multivariate discriminants are used to distinguish signal events from background events.

The data are in good agreement with the SM expectations, and no evidence of a signal is found. Limits at 95% CL are placed on the $t \to Zq$ branching ratios for both the tZu and tZc vertices and for both the RH and LH couplings. Assuming a LH coupling, the observed limits on the branching ratios are 6.2×10^{-5} for $t \to Zu$ and 13×10^{-5} for $t \to Zc$. These results for $t \to Zu$ ($t \to Zc$) improve on the previous observed limits from ATLAS by a factor of 3 (2), and on the previous expected limits by a factor of 5 (3). These are the most stringent limits to date. The improvement relative to the previous results comes from the inclusion of the FCNC-in-single-top-quark-production signal and the usage of a multivariate analysis in addition to the higher integrated luminosity. These results also constrain the values of Wilson coefficients for effective field theory operators contributing to the $t \to Zu$ and $t \to Zc$ FCNC decays of the top quark.

References

[1] Particle Data Group, *Review of Particle Physics*, PTEP **2020** (2020) 083C01.

[2] S. L. Glashow, J. Iliopoulos, and L. Maiani, *Weak Interactions with Lepton-Hadron Symmetry*, Phys. Rev. D **2** (1970) 1285.

[3] J. A. Aguilar-Saavedra, *Top flavour-changing neutral interactions: theoretical expectations and experimental detection*, Acta Phys. Polon. B **35** (2004) 2695, arXiv: hep-ph/0409342.

[4] J. A. Aguilar-Saavedra, *Effects of mixing with quark singlets*, Phys. Rev. D **67** (2003) 035003, arXiv: hep-ph/0210112, [Erratum: Phys. Rev. D **69** (2004) 099901].

[5] D. Atwood, L. Reina, and A. Soni, *Phenomenology of two Higgs doublet models with flavor-changing neutral currents*, Phys. Rev. D **55** (1997) 3156, arXiv: hep-ph/9609279.

[6] J. J. Cao et al., *Supersymmetry-induced flavor-changing neutral-current top-quark processes at the CERN Large Hadron Collider*, Phys. Rev. D **75** (2007) 075021, arXiv: hep-ph/0702264.

[7] J. M. Yang, B.-L. Young, and X. Zhang, *Flavor-changing top quark decays in R-parity-violating supersymmetric models*, Phys. Rev. D **58** (1998) 055001, arXiv: hep-ph/9705341.

[8] K. Agashe, G. Perez, and A. Soni, *Collider signals of top quark flavor violation from a warped extra dimension*, Phys. Rev. D **75** (2007) 015002, arXiv: hep-ph/0606293.

[9] P. Q. Hung, Y.-X. Lin, C. S. Nugroho, and T.-C. Yuan, *Top quark rare decays via loop-induced FCNC interactions in extended mirror fermion model*, Nucl. Phys. B **927** (2018) 166, arXiv: 1709.01690 [hep-ph].

[10] J. A. Aguilar-Saavedra, *A minimal set of top anomalous couplings*, Nucl. Phys. B **812** (2009) 181, arXiv: 0811.3842 [hep-ph].

[11] G. Durieux, F. Maltoni, and C. Zhang, *Global approach to top-quark flavor-changing interactions*, Phys. Rev. D **91** (2015) 074017, arXiv: 1412.7166 [hep-ph].

[12] B. Grzadkowski, M. Iskrzynski, M. Misiak, and J. Rosiek, *Dimension-six terms in the Standard Model Lagrangian*, JHEP **10** (2010) 085, arXiv: 1008.4884 [hep-ph].

[13] OPAL Collaboration, *Search for single top quark production at LEP2*, Phys. Lett. B **521** (2001) 181, arXiv: hep-ex/0110009.

[14] ALEPH Collaboration, *Search for single top production in e^+e^- collisions at $\sqrt{s}$ up to 209 GeV*, Phys. Lett. B **543** (2002) 173, arXiv: hep-ex/0206070.

[15] L3 Collaboration, *Search for single top production at LEP*, Phys. Lett. B **549** (2002) 290, arXiv: hep-ex/0210041.

[16] DELPHI Collaboration, *Search for single top production via FCNC at LEP at $\sqrt{s}$ = 189-208 GeV*, Phys. Lett. B **590** (2004) 21, arXiv: hep-ex/0404014.

[17] ZEUS Collaboration, *Search for single-top production in ep collisions at HERA*, Phys. Lett. B **708** (2012) 27, arXiv: 1111.3901 [hep-ex].

[18] CDF Collaboration,
Search for the Flavor-Changing Neutral-Current Decay $t \to Zq$ in $p\bar{p}$ Collisions at $\sqrt{s} = 1.96$ TeV,
Phys. Rev. Lett. **101** (2008) 192002, arXiv: 0805.2109 [hep-ex].

[19] D0 Collaboration, *Search for flavor changing neutral currents in decays of top quarks*,
Phys. Lett. B **701** (2011) 313, arXiv: 1103.4574 [hep-ex].

[20] ATLAS Collaboration, *Search for flavour-changing neutral current top-quark decays to qZ in pp collision data collected with the ATLAS detector at $\sqrt{s} = 8$ TeV*, Eur. Phys. J. C **76** (2016) 12,
arXiv: 1508.05796 [hep-ex].

[21] ATLAS Collaboration, *Search for flavour-changing neutral current top-quark decays $t \to qZ$ in proton–proton collisions at $\sqrt{s} = 13$ TeV with the ATLAS detector*, JHEP **07** (2018) 176,
arXiv: 1803.09923 [hep-ex].

[22] CMS Collaboration, *Search Search for Flavor-Changing Neutral Currents in Top-Quark Decays $t \to Zq$ in pp Collisions at $\sqrt{s} = 8$ TeV*, Phys. Rev. Lett. **112** (2014) 171802,
arXiv: 1312.4194 [hep-ex].

[23] CMS Collaboration, *Search for associated production of a Z boson with a single top quark and for tZ flavour-changing interactions in pp collisions at $\sqrt{s} = 8$ TeV*, JHEP **07** (2017) 003,
arXiv: 1702.01404 [hep-ex].

[24] ATLAS Collaboration, *The ATLAS Experiment at the CERN Large Hadron Collider*,
JINST **3** (2008) S08003.

[25] ATLAS Collaboration, *Performance of the ATLAS trigger system in 2015*,
Eur. Phys. J. C **77** (2017) 317, arXiv: 1611.09661 [hep-ex].

[26] ATLAS Collaboration, *The ATLAS Collaboration Software and Firmware*,
ATL-SOFT-PUB-2021-001, 2021, URL: https://cds.cern.ch/record/2767187.

[27] ATLAS Collaboration,
ATLAS data quality operations and performance for 2015–2018 data-taking,
JINST **15** (2020) P04003, arXiv: 1911.04632 [physics.ins-det].

[28] ATLAS Collaboration, *Performance of electron and photon triggers in ATLAS during LHC Run 2*,
Eur. Phys. J. C **80** (2020) 47, arXiv: 1909.00761 [hep-ex].

[29] ATLAS Collaboration, *Performance of the ATLAS muon triggers in Run 2*,
JINST **15** (2020) P09015, arXiv: 2004.13447 [hep-ex].

[30] GEANT4 Collaboration, *GEANT4 – a simulation toolkit*, Nucl. Instrum. Meth. A **506** (2003) 250.

[31] ATLAS Collaboration, *The ATLAS Simulation Infrastructure*, Eur. Phys. J. C **70** (2010) 823,
arXiv: 1005.4568 [physics.ins-det].

[32] D. J. Lange, *The EvtGen particle decay simulation package*,
Nucl. Instrum. Meth. A **462** (2001) 152.

[33] T. Sjöstrand, S. Mrenna, and P. Skands, *A brief introduction to PYTHIA 8.1*,
Comput. Phys. Commun. **178** (2008) 852, arXiv: 0710.3820 [hep-ph].

[34] ATLAS Collaboration, *The Pythia 8 A3 tune description of ATLAS minimum bias and inelastic measurements incorporating the Donnachie–Landshoff diffractive model*,
ATL-PHYS-PUB-2016-017, 2016, URL: https://cds.cern.ch/record/2206965.

[35] R. D. Ball et al., *Parton distributions with LHC data*, Nucl. Phys. B **867** (2013) 244,
arXiv: 1207.1303 [hep-ph].

[36] J. Alwall et al., *The automated computation of tree-level and next-to-leading order differential cross sections, and their matching to parton shower simulations*, JHEP **07** (2014) 079, arXiv: 1405.0301 [hep-ph].

[37] R. D. Ball et al., *Parton distributions for the LHC run II*, JHEP **04** (2015) 040, arXiv: 1410.8849 [hep-ph].

[38] ATLAS Collaboration, *ATLAS Pythia 8 tunes to 7 TeV data*, ATL-PHYS-PUB-2014-021, 2014, URL: https://cds.cern.ch/record/1966419.

[39] A. Alloul, N. D. Christensen, C. Degrande, C. Duhr, and B. Fuks, *FeynRules 2.0 – A complete toolbox for tree-level phenomenology*, Comput. Phys. Commun. **185** (2014) 2250, arXiv: 1310.1921 [hep-ph].

[40] C. Degrande, F. Maltoni, J. Wang, and C. Zhang, *Automatic computations at next-to-leading order in QCD for top-quark flavor-changing neutral processes*, Phys. Rev. D **91** (2015) 034024, arXiv: 1412.5594 [hep-ph].

[41] M. Bähr et al., *Herwig++ physics and manual*, Eur. Phys. J. C **58** (2008) 639, arXiv: 0803.0883 [hep-ph].

[42] J. Bellm et al., *Herwig 7.0/Herwig++ 3.0 release note*, Eur. Phys. J. C **76** (2016) 196, arXiv: 1512.01178 [hep-ph].

[43] J. Bellm et al., *Herwig 7.1 Release Note*, (2017), arXiv: 1705.06919 [hep-ph].

[44] L. A. Harland-Lang, A. D. Martin, P. Motylinski, and R. S. Thorne, *Parton distributions in the LHC era: MMHT 2014 PDFs*, Eur. Phys. J. C **75** (2015) 204, arXiv: 1412.3989 [hep-ph].

[45] M. Beneke, P. Falgari, S. Klein, and C. Schwinn, *Hadronic top-quark pair production with NNLL threshold resummation*, Nucl. Phys. B **855** (2012) 695, arXiv: 1109.1536 [hep-ph].

[46] M. Cacciari, M. Czakon, M. Mangano, A. Mitov, and P. Nason, *Top-pair production at hadron colliders with next-to-next-to-leading logarithmic soft-gluon resummation*, Phys. Lett. B **710** (2012) 612, arXiv: 1111.5869 [hep-ph].

[47] P. Bärnreuther, M. Czakon, and A. Mitov, *Percent-Level-Precision Physics at the Tevatron: Next-to-Next-to-Leading Order QCD Corrections to $q\bar{q} \to t\bar{t} + X$*, Phys. Rev. Lett. **109** (2012) 132001, arXiv: 1204.5201 [hep-ph].

[48] M. Czakon and A. Mitov, *NNLO corrections to top-pair production at hadron colliders: the all-fermionic scattering channels*, JHEP **12** (2012) 054, arXiv: 1207.0236 [hep-ph].

[49] M. Czakon and A. Mitov, *NNLO corrections to top pair production at hadron colliders: the quark-gluon reaction*, JHEP **01** (2013) 080, arXiv: 1210.6832 [hep-ph].

[50] M. Czakon, P. Fiedler, and A. Mitov, *Total Top-Quark Pair-Production Cross Section at Hadron Colliders Through $O(\alpha_S^4)$*, Phys. Rev. Lett. **110** (2013) 252004, arXiv: 1303.6254 [hep-ph].

[51] M. Czakon and A. Mitov, *Top++: A program for the calculation of the top-pair cross-section at hadron colliders*, Comput. Phys. Commun. **185** (2014) 2930, arXiv: 1112.5675 [hep-ph].

[52] S. Frixione, G. Ridolfi, and P. Nason,
A positive-weight next-to-leading-order Monte Carlo for heavy flavour hadroproduction,
JHEP **09** (2007) 126, arXiv: 0707.3088 [hep-ph].

[53] P. Nason, *A new method for combining NLO QCD with shower Monte Carlo algorithms*,
JHEP **11** (2004) 040, arXiv: hep-ph/0409146.

[54] S. Frixione, P. Nason, and C. Oleari,
Matching NLO QCD computations with parton shower simulations: the POWHEG method,
JHEP **11** (2007) 070, arXiv: 0709.2092 [hep-ph].

[55] S. Alioli, P. Nason, C. Oleari, and E. Re, *A general framework for implementing NLO calculations in shower Monte Carlo programs: the POWHEG BOX*, JHEP **06** (2010) 043,
arXiv: 1002.2581 [hep-ph].

[56] H. B. Hartanto, B. Jäger, L. Reina, and D. Wackeroth,
Higgs boson production in association with top quarks in the POWHEG BOX,
Phys. Rev. D **91** (2015) 094003, arXiv: 1501.04498 [hep-ph].

[57] ATLAS Collaboration, *Studies on top-quark Monte Carlo modelling for Top2016*,
ATL-PHYS-PUB-2016-020, 2016, URL: https://cds.cern.ch/record/2216168.

[58] T. Sjöstrand et al., *An introduction to PYTHIA 8.2*, Comput. Phys. Commun. **191** (2015) 159,
arXiv: 1410.3012 [hep-ph].

[59] ATLAS Collaboration,
Improvements in $t\bar{t}$ modelling using NLO+PS Monte Carlo generators for Run 2,
ATL-PHYS-PUB-2018-009, 2018, URL: https://cds.cern.ch/record/2630327.

[60] E. Re,
Single-top Wt-channel production matched with parton showers using the POWHEG method,
Eur. Phys. J. C **71** (2011) 1547, arXiv: 1009.2450 [hep-ph].

[61] S. Frixione, E. Laenen, P. Motylinski, C. White, and B. R. Webber,
Single-top hadroproduction in association with a W boson, JHEP **07** (2008) 029,
arXiv: 0805.3067 [hep-ph].

[62] F. Demartin, B. Maier, F. Maltoni, K. Mawatari, and M. Zaro,
tWH associated production at the LHC, Eur. Phys. J. C **77** (2017) 34,
arXiv: 1607.05862 [hep-ph].

[63] S. Alioli, P. Nason, C. Oleari, and E. Re,
NLO vector-boson production matched with shower in POWHEG, JHEP **07** (2008) 060,
arXiv: 0805.4802 [hep-ph].

[64] ATLAS Collaboration, *Measurement of the Z/γ^* boson transverse momentum distribution in pp collisions at $\sqrt{s} = 7$ TeV with the ATLAS detector*, JHEP **09** (2014) 145,
arXiv: 1406.3660 [hep-ex].

[65] H.-L. Lai et al., *New parton distributions for collider physics*, Phys. Rev. D **82** (2010) 074024,
arXiv: 1007.2241 [hep-ph].

[66] J. Pumplin et al.,
New Generation of Parton Distributions with Uncertainties from Global QCD Analysis,
JHEP **07** (2002) 012, arXiv: hep-ph/0201195.

[67] P. Golonka and Z. Was,
PHOTOS Monte Carlo: a precision tool for QED corrections in Z and W decays,
Eur. Phys. J. C **45** (2006) 97, arXiv: hep-ph/0506026.

[68] N. Davidson, T. Przedzinski, and Z. Was,
PHOTOS Interface in C++: Technical and physics documentation,
Comput. Phys. Commun. **199** (2016) 86, arXiv: 1011.0937 [hep-ph].

[69] E. Bothmann et al., *Event generation with Sherpa 2.2*, SciPost Phys. **7** (2019) 034,
arXiv: 1905.09127 [hep-ph].

[70] T. Gleisberg and S. Höche, *Comix, a new matrix element generator*, JHEP **12** (2008) 039,
arXiv: 0808.3674 [hep-ph].

[71] S. Schumann and F. Krauss,
A parton shower algorithm based on Catani–Seymour dipole factorisation, JHEP **03** (2008) 038,
arXiv: 0709.1027 [hep-ph].

[72] S. Höche, F. Krauss, M. Schönherr, and F. Siegert,
A critical appraisal of NLO+PS matching methods, JHEP **09** (2012) 049,
arXiv: 1111.1220 [hep-ph].

[73] S. Höche, F. Krauss, M. Schönherr, and F. Siegert,
QCD matrix elements + parton showers. The NLO case, JHEP **04** (2013) 027,
arXiv: 1207.5030 [hep-ph].

[74] S. Catani, F. Krauss, B. R. Webber, and R. Kuhn, *QCD Matrix Elements + Parton Showers*,
JHEP **11** (2001) 063, arXiv: hep-ph/0109231.

[75] S. Höche, F. Krauss, S. Schumann, and F. Siegert, *QCD matrix elements and truncated showers*,
JHEP **05** (2009) 053, arXiv: 0903.1219 [hep-ph].

[76] F. Buccioni et al., *OpenLoops 2*, Eur. Phys. J. C **79** (2019) 866, arXiv: 1907.13071 [hep-ph].

[77] F. Cascioli, P. Maierhöfer, and S. Pozzorini, *Scattering Amplitudes with Open Loops*,
Phys. Rev. Lett. **108** (2012) 111601, arXiv: 1111.5206 [hep-ph].

[78] A. Denner, S. Dittmaier, and L. Hofer,
Collier: A fortran-based complex one-loop library in extended regularizations,
Comput. Phys. Commun. **212** (2017) 220, arXiv: 1604.06792 [hep-ph].

[79] P. Nason and G. Zanderighi, *W^+W^-, WZ and ZZ production in the POWHEG-BOX-V2*,
Eur. Phys. J. C **74** (2014) 2702, arXiv: 1311.1365 [hep-ph].

[80] ATLAS Collaboration, *Vertex Reconstruction Performance of the ATLAS Detector at $\sqrt{s}$ = 13 TeV*,
ATL-PHYS-PUB-2015-026, 2015, URL: https://cds.cern.ch/record/2037717.

[81] ATLAS Collaboration, *Electron and photon performance measurements with the ATLAS detector using the 2015–2017 LHC proton–proton collision data*, JINST **14** (2019) P12006,
arXiv: 1908.00005 [hep-ex].

[82] ATLAS Collaboration, *Evidence for the associated production of the Higgs boson and a top quark pair with the ATLAS detector*, Phys. Rev. D **97** (2018) 072003, arXiv: 1712.08891 [hep-ex].

[83] ATLAS Collaboration, *Muon reconstruction and identification efficiency in ATLAS using the full Run 2 pp collision data set at $\sqrt{s}$ = 13 TeV*, Eur. Phys. J. C **81** (2021) 578,
arXiv: 2012.00578 [hep-ex].

[84] ATLAS Collaboration,
Jet reconstruction and performance using particle flow with the ATLAS Detector,
Eur. Phys. J. C **77** (2017) 466, arXiv: 1703.10485 [hep-ex].

[85] M. Cacciari, G. P. Salam, and G. Soyez, *The anti-k_t jet clustering algorithm*, JHEP **04** (2008) 063,
arXiv: 0802.1189 [hep-ph].

[86] M. Cacciari, G. P. Salam, and G. Soyez, *FastJet user manual*, Eur. Phys. J. C **72** (2012) 1896,
arXiv: 1111.6097 [hep-ph].

[87] ATLAS Collaboration, *Jet energy scale and resolution measured in proton–proton collisions at $\sqrt{s} = 13$ TeV with the ATLAS detector*, Eur. Phys. J. C **81** (2020) 689,
arXiv: 2007.02645 [hep-ex].

[88] ATLAS Collaboration, *Performance of pile-up mitigation techniques for jets in pp collisions at $\sqrt{s} = 8$ TeV using the ATLAS detector*, Eur. Phys. J. C **76** (2016) 581,
arXiv: 1510.03823 [hep-ex].

[89] ATLAS Collaboration, *ATLAS flavour-tagging algorithms for the LHC Run 2 pp collision dataset*, (2022), arXiv: 2211.16345 [physics.data-an].

[90] ATLAS Collaboration, *Performance of missing transverse momentum reconstruction with the ATLAS detector using proton–proton collisions at $\sqrt{s} = 13$ TeV*, Eur. Phys. J. C **78** (2018) 903,
arXiv: 1802.08168 [hep-ex].

[91] ATLAS Collaboration,
E_T^{miss} performance in the ATLAS detector using 2015–2016 LHC pp collisions,
ATLAS-CONF-2018-023, 2018, URL: https://cds.cern.ch/record/2625233.

[92] ATLAS Collaboration, *Measurement of the top-quark mass using a leptonic invariant mass in pp collisions at $\sqrt{s} = 13$ TeV with the ATLAS detector*, (2022), arXiv: 2209.00583 [hep-ex].

[93] A. D. Bukin, *Fitting function for asymmetric peaks*, 2007,
arXiv: 0711.4449 [physics.data-an].

[94] A. Kulesza, L. Motyka, T. Stebel, and V. Theeuwes,
Soft gluon resummation for associated $t\bar{t}H$ production at the LHC, JHEP **03** (2016) 065,
arXiv: 1509.02780 [hep-ph].

[95] J. H. Friedman, *Stochastic gradient boosting*, Comput. Stat. Data Anal. **38** (2002) 367.

[96] A. Hoecker et al., *TMVA - Toolkit for Multivariate Data Analysis*, 2007,
arXiv: physics/0703039 [physics.data-an].

[97] L. Breiman, J. Friedman, C. Stone, and R. Olshen, *Classification and Regression Trees*,
Chapman & Hall, 1984.

[98] ATLAS Collaboration, *Jet energy scale measurements and their systematic uncertainties in proton–proton collisions at $\sqrt{s} = 13$ TeV with the ATLAS detector*, Phys. Rev. D **96** (2017) 072002,
arXiv: 1703.09665 [hep-ex].

[99] ATLAS Collaboration, *ATLAS b-jet identification performance and efficiency measurement with $t\bar{t}$ events in pp collisions at $\sqrt{s} = 13$ TeV*, Eur. Phys. J. C **79** (2019) 970,
arXiv: 1907.05120 [hep-ex].

[100] ATLAS Collaboration, *Measurement of b-tagging efficiency of c-jets in $t\bar{t}$ events using a likelihood approach with the ATLAS detector*, ATLAS-CONF-2018-001, 2018,
URL: https://cds.cern.ch/record/2306649.

[101] ATLAS Collaboration, *Calibration of light-flavour b-jet mistagging rates using ATLAS proton–proton collision data at* $\sqrt{s}$ = 13 *TeV*, ATLAS-CONF-2018-006, 2018, URL: https://cds.cern.ch/record/2314418.

[102] J. Butterworth et al., *PDF4LHC recommendations for LHC Run II*, J. Phys. G **43** (2016) 023001, arXiv: 1510.03865 [hep-ph].

[103] A. D. Martin, W. J. Stirling, R. S. Thorne, and G. Watt, *Parton distributions for the LHC*, Eur. Phys. J. C **63** (2009) 189, arXiv: 0901.0002 [hep-ph].

[104] A. D. Martin, W. J. Stirling, R. S. Thorne, and G. Watt, *Uncertainties on* α_S *in global PDF analyses and implications for predicted hadronic cross sections*, Eur. Phys. J. C **64** (2009) 653, arXiv: 0905.3531 [hep-ph].

[105] J. Gao et al., *CT10 next-to-next-to-leading order global analysis of QCD*, Phys. Rev. D **89** (2014) 033009, arXiv: 1302.6246 [hep-ph].

[106] LHC Higgs Cross Section Working Group, *Handbook of LHC Higgs Cross Sections: 4. Deciphering the Nature of the Higgs Sector*, CERN-2017-002-M (CERN, Geneva, 2016), arXiv: 1610.07922 [hep-ph].

[107] ATLAS Collaboration, *Evidence for* $t\bar{t}t\bar{t}$ *production in the multilepton final state in proton–proton collisions at* $\sqrt{s}$ = 13*TeV with the ATLAS detector*, Eur. Phys. J. C **80** (2020) 1085, arXiv: 2007.14858 [hep-ex].

[108] ATLAS Collaboration, *Observation of the associated production of a top quark and a Z boson in* pp *collisions at* $\sqrt{s}$ = 13 *TeV with the ATLAS detector*, JHEP **07** (2020) 124, arXiv: 2002.07546 [hep-ex].

[109] CMS Collaboration, *Measurement of the associated production of a single top quark and a Z boson in* pp *collisions at* $\sqrt{s}$ = 13 *TeV*, Phys. Lett. B **779** (2018) 358, arXiv: 1712.02825 [hep-ex].

[110] ATLAS Collaboration, *Measurement of* $W^{\pm}Z$ *production cross sections and gauge boson polarisation in* pp *collisions at* $\sqrt{s}$ = 13 *TeV with the ATLAS detector*, Eur. Phys. J. C **79** (2019) 535, arXiv: 1902.05759 [hep-ex].

[111] ATLAS Collaboration, *Evidence for the* $H \to b\bar{b}$ *decay with the ATLAS detector*, JHEP **12** (2017) 024, arXiv: 1708.03299 [hep-ex].

[112] ATLAS Collaboration, *Luminosity determination in* pp *collisions at* $\sqrt{s}$ = 13 *TeV using the ATLAS detector at the LHC*, ATLAS-CONF-2019-021, 2019, URL: https://cds.cern.ch/record/2677054.

[113] G. Avoni et al., *The new LUCID-2 detector for luminosity measurement and monitoring in ATLAS*, JINST **13** (2018) P07017.

[114] A. L. Read, *Presentation of search results: the* CL_S *technique*, J. Phys. G **28** (2002) 2693.

[115] G. Cowan, K. Cranmer, E. Gross, and O. Vitells, *Asymptotic formulae for likelihood-based tests of new physics*, Eur. Phys. J. C **71** (2011) 1554, arXiv: 1007.1727 [physics.data-an], Erratum: Eur. Phys. J. C **73** (2013) 2501.